Photothermally heated and mesh-gridded solar-driven direct contact membrane distillation for high saline water desalination

Milad Shokrollahi[1], Mahdieh Asadollahi[2], Seyyed Abbas Mousavi[2,*], Abbas Rajabi-ghahnavieh[1],
Mohammad Behzadi-Sarok[3], Mohamed Khayet[4,5**]

[1] Department of Energy Engineering, Sharif University of Technology, Azadi Ave., Tehran, Iran
[2] Department of Chemical and Petroleum Engineering, Sharif University of Technology, Azadi Ave., Tehran, Iran
[3]Department of Mechanical Engineering, Sharif University of Technology, Azadi Ave., Tehran, Iran
[4]Department of Structure of Matter, Thermal Physics and Electronics, Faculty of Physics, University Complutense of Madrid, Avda. Complutense s/n, 28040 Madrid, Spain
[5]Madrid Institute for Advanced Studies of Water (IMDEA Water Institute), Calle Punto Net N° 4, 28805 Alcalá de Henares, Madrid, Spain

**Corresponding Author: E-mail: musavi@sharif.ir, Tel.: +98 2166166427, Fax: +98 2166022853*
***Corresponding Author: E-mail: khayetm@fis.ucm.es, Tel.: +34 913945185*

Abstract

Photothermally heated and mesh-gridded membrane distillation (PHMD) system is proposed for desalination of high saline aqueous solutions. A triple-layered membrane, composed of a photothermal top nanofibrous layer containing polyacrylonitrile and dispersed carbon black nanoparticles and a polyvinylidene fluoride porous membrane supported on a nonwoven polyester, was prepared. A polypropylene mesh was used to hold the membrane. A 3D numerical simulation of the PHMD system was carried out by COMSOL and the appropriate length of the membrane module was determined. The effects of various operating parameters including solar radiation intensity on the permeate flux and thermal efficiency were investigated. The increase of the feed flow rate reduced both the permeate flux and the thermal efficiency due to the reduction of the residence time of the feed solution on the photothermal membrane module. In addition, the increase of the solar radiation intensity from 500 to 1100 W/m^2 and the ambient temperature from 293 to 313 K resulted in a significant enhancement of the permeate flux and thermal efficiency. In general, good agreements were found between the experimental and simulated results.

Keywords: Membrane distillation; Desalination; Photothermal membrane; Solar energy; High saline water; Thermal efficiency.

1. Introduction

One of the most important challenges that humans face nowadays is water scarcity, which is the result of population growth, urbanization, climate change and exhaustion of limited freshwater resources [1]. Desalination processes are generally considered the only feasible option to solve this issue by means of thermally based technologies consisting of liquid/vapor phase change mechanism (e.g. multi-stage flash, MSF and multi-effect distillation, MED) or isothermal membrane separation technologies (e.g. reverse osmosis, RO and electrodialysis ED). The thermally based methods display great capital and operational costs and require a high amount of energy consumption whereas the isothermal membrane based methods, such as the pressure-driven membrane separation RO, are much more energy efficient, necessitate smaller space but suffer from distinct drawbacks such as membrane fouling, which reduces water production and increase the specific energy consumption [2-4].

The non-isothermal membrane technology of emerging interest, membrane distillation (MD), exhibits outstanding characteristics in desalination field as it combines both thermal and membrane based benefits (e.g. very high salt rejection factor greater than 99.99%, possibility to treat high saline solutions near saturation such as brines, operation at lower temperatures (below the boiling points of feed aqueous solutions) than those applied in thermally based technologies, use of waster energy or renewable energies, less membrane fouling effect compared to the pressure-driven membrane processes as the hydrostatic pressure applied in MD is near the atmospheric pressure) [5-8].

It is to be noted that the most widely used and studied MD configuration is the direct contact membrane distillation (DCMD) variant in which both surfaces of the porous hydrophobic membrane are brought in direct contact with the hot feed and cold permeate aqueous solutions. The applied temperature difference between both sides of the membrane induces the necessary driving force, water vapor pressure difference, for evaporation of water molecules at the hot liquid/vapor interface formed at the feed/membrane surface and their condensation at the cold liquid/vapor interface formed at the permeate/membrane surface [9,10]. It must be mentioned that the pores of the membrane must be maintained always dry so that the liquid entry pressure (*LEP*) of the membrane must be as high as possible with high porosity and pore sizes ranging from 10 nm to 1 μm with low thermal conductivity [11]. Despite the aforementioned advantages, MD process suffers from some limitations like the temperature polarization (*TP*) and concentration polarization (*CP*) effects reducing the applied driving force, the risk of membrane pore wetting reducing the quality of the produced water, high heat transfer by conduction reducing the thermal efficiency of the MD process and increasing the specific energy consumption [12].

Different hydrophobic polymers are used for the preparation of MD membranes such as polypropylene (PP) [13,14], polytetrafluoroethylene (PTFE) [15] and polyvinylidene fluoride (PVDF) [16,17]. Among these materials, PVDF is one of the commonly used polymers because of its high chemical and thermal resistance and its easy use for the formation of membranes by the simple non-solvent induced phase inversion (NIPS) method [18,19].

In MD systems, continuous heating of the feed solution must be guaranteed in order to establish the required driving force for water production. Other than low-temperature industrial waste heat, one of the used renewable energy sources is solar energy. This inexhaustible renewable energy source demands materials with specific absorbance and transmittance properties as well as a high energy conversion ability [20, 21]. In conventional MD solar systems, heating the feed aqueous solution to be treated by MD is accomplished before its entrance in membrane modules by means of solar thermal collectors [22,23]. During last decade, direct solar radiation of MD membrane modules has been proposed to heat up the feed aqueous solution while circulating tangentially on adequately tailored photothermal MD membrane surfaces [24-26] or by the application of photothermal nanofluids as feed aqueous saline solution to improve MD water production rate [27].

When photothermal materials are subjected to light, the generation of heat occurs at the interface of the feed/membrane surface increasing its temperature. Therefore, water molecules evaporate at this feed/membrane interface cross the dried pores in vapor phase to finally condense at the cold permeate/membrane surface. One of the advantages of this approach is the low *TP* effect in the membrane module. In addition, it is not necessary to preheat the bulk feed solution with external heaters reducing considerably the specific energy consumption as consequence.

Politano et al. [28], who prepared mixed matrix membranes (MMMs) by incorporating silver nanoparticles (Ag NPs) in PVDF for MD applications, showed that ultraviolet (UV) irradiation (23 kW/m^2) of MMMs led to plasmonic excitation of the Ag NPs, which resulted in heating of membrane surface, reduced *TP* effect and enhanced water permeate by about 9 to 11-fold over that of the pristine membrane. Dongare et al. [29] fabricated a dual layered membrane consisting of carbon black nanoparticles (CB NPs) filled hydrophilic polyvinyl alcohol (PVA) layer coated on commercial hydrophobic PVDF membrane as a supporting layer. Under laminar flow operation, the results proved that CB NPs used as a photothermal material heated the membrane surface locally under solar radiation and increased the MD performance. In another research, commercial PVDF membranes were coated by two types of photothermal nanomaterials, CB NPs using an evaporation coating method and attachment of SiO_2/Au nanoshells (NSs) using polydopamine (PDA) as binder [30]. Upon irradiation by simulated sunlight, the CB NPs and SiO_2/Au NSs showed noticeable photothermal effects reducing the TP because of the direct surface heating and increasing significantly the MD permeate flux (i.e. up to 33%). PDA was also coated on a commercial PVDF membrane via a self-polymerization process for MD [31]. It is to be noted that PDA has a wide light absorption and a considerable photothermal conversion together with a remarkable adhesion propensity to polymeric membrane surfaces. It was reported that PDA coated membranes exhibited outstanding solar MD performance (i.e. 45% efficiency under 0.75 kW/m^2 irradiation).

In addition to the above mentioned experimental research studies, simulation of MD systems has also attracted much attention and various theoretical models including computational fluid dynamics (CFD) models were proposed [32-34]. The developed CFD models describe the mass, momentum, and heat transfer in the feed and permeate channels of MD systems. The MD permeate flux together with the temperature and concentration profiles (i.e. *TP* and *CP*) have been analyzed in terms of different operating parameters such as the concentration of feed solution, the feed flow rate, the feed temperature, and the arrangement of the feed and permeate circulation in the membrane module (i.e. co-current or counter-current modes) besides the membrane characteristics including its thickness, pore size, and length in the module [35-41].

The main objective of the present research study is to design and construct a novel photothermally heated and mesh-gridded solar-driven direct contact membrane distillation (PHMD) system for high saline water desalination (Fig. 1). One of the benefits of this approach is to reduce the *TP* effect in the membrane module as the temperature of the feed saline solution at the membrane/feed interface (T_{mh}) is kept higher than that of the bulk feed (T_{bh}) because of the localized heating of the membrane surface. The photothermal membrane prepared for this system is a triple-layered membrane formed by a polyacrylonitrile (PAN) top layer containing dispersed CB NPs that was coated on the surface of supported phase inversion PVDF membrane using a nonwoven polyester (PL). To improve the performance of the photothermal membrane, turbulent flow was induced in both the feed and permeate channels using polypropylene (PP) mesh grid that also stabilizes the membrane between the feed and permeate channels.

Fig 1(a) shows the temperature profile of the PHMD system. The feed enters the membrane module without preheating and as it circulates over the membrane surface it is heated up because of the photothermal characteristic of the top membrane layer. The permeate liquid also enters the membrane module at ambient temperature and while it circulates through the permeate side of the membrane its temperature is increased because of the heat transferred by conduction through the membrane from the feed to the permeate side plus the heat associated to mass transfer. The temperature profile of the conventional MD system (Fig. 1(b)) is different from that of the PHMD system since in the conventional MD system the feed is heated up outside the membrane module and its temperature decreases while it circulates through the feed membrane surface.

In addition, prior its construction, the design of the PHMD system was first optimized by a three-dimensional (3D) CFD simulation model in a counter-current arrangement. The results permit to determine the appropriate length of the photothermal membrane module and the performance of the PHMD system was then investigated.

The effects of various operating parameters such as the feed concentration, feed and permeate flow rates, and the solar radiation intensity and the ambient temperature on the permeate flux and thermal efficiency (TE) were investigated and the obtained experimental data were compared with the simulated ones and with those obtained with a conventional MD system as shown in Fig. 1.

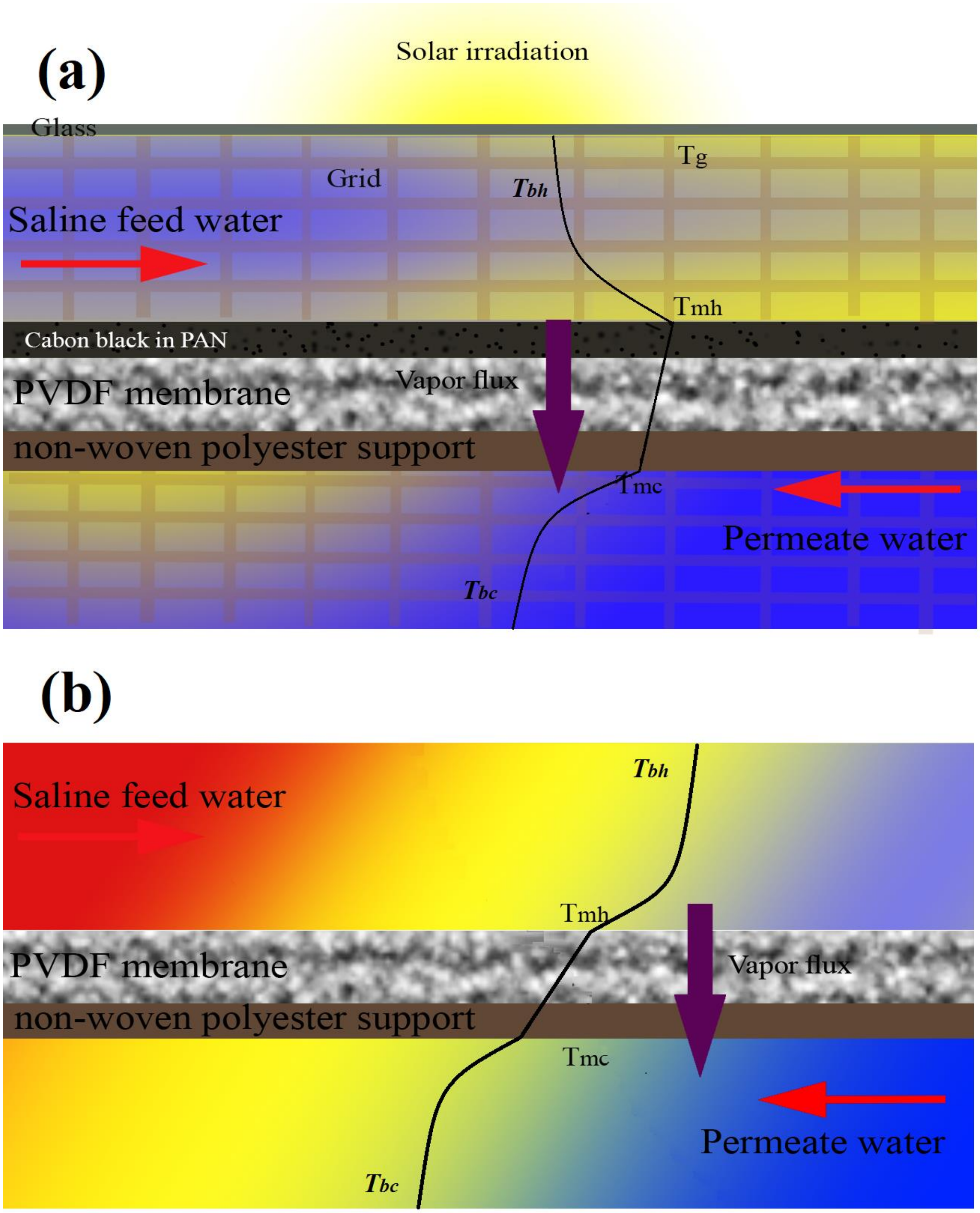

Fig. 1. Comparison of temperature profile of (a) PHMD system with (b) conventional MD system. (T_g: glass temperature; T_{bh}: bulk feed temperature; T_{mh}: membrane/feed interface temperature; T_{mc}: membrane/permeate interface temperature; T_{bc}: bulk permeate temperature).

2. Numerical modeling and simulation

For the description of vapor transport through the PHMD system, a comprehensive numerical approach was developed and applied. The flat sheet membrane was maintained between PP mesh grids in the membrane module inducing turbulent flow in both the feed and permeate channels. Three-coupled transport equations including mass, momentum, and energy were numerically solved using the known Finite Element Method (FEM). All simulations were performed in a 3D framework with the aid of COMSOL Multiphysics v5.4.

The model of the membrane module used in CFD simulation is shown in Fig. 2. This contains three domains: feed channel, membrane and permeate channel. Provided that the counter-current mode was adopted, the feed and permeate flows were introduced in the membrane module at the positions x=0 (x_0) and x=L (x_L), respectively.

For sake of model simplicity, the considered assumptions were:

- Steady state process
- Consideration of feed and permeate as incompressible liquid
- Turbulent flow in both the feed and permeate sides of the membrane
- Dependence of mass transfer only on the temperature difference
- No chemical reaction
- Negligible heat loss to the surroundings
- No water transport through the membrane pores (only vapor transport)

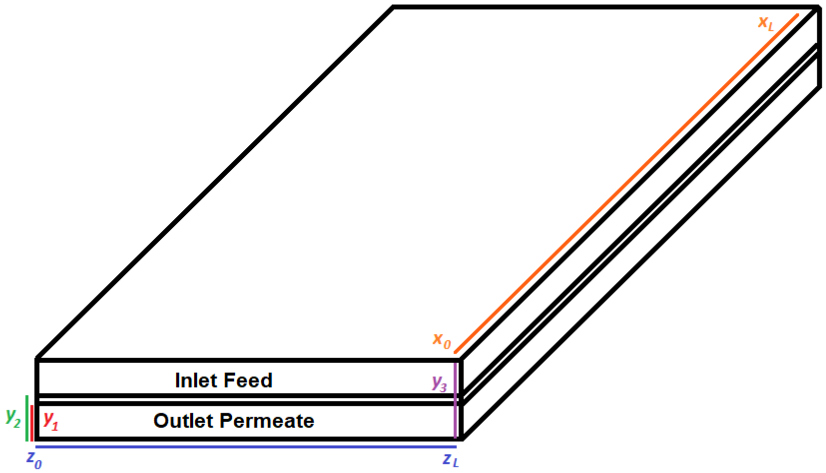

Fig. 2. Model of membrane module used in the PHMD system.

2.1. Governing equations of the developed model

The governing equations together with the boundary conditions of the feed channel, membrane, and permeate channel domains are detailed in the following sections.

2.1.1. Feed channel

Taking into consideration the previously mentioned assumptions, the mass transfer in the feed side contains terms of the convection-diffusion transport of water as [42]:

$$u_j \frac{\partial C_h}{\partial x_j} = \frac{\partial}{\partial x_k}(D_h \frac{\partial C_h}{\partial x_k}) \tag{1}$$

where C_h, u_j, D_h are the concentration, velocity of the *j^th^* component, and diffusion coefficient of saline water, respectively. The water mass flux is calculated using Fick's first law equation [43]. Based on Reynolds's definition, each parameter (e.g. ϕ) can be specified by summating the averaged part ($\bar{\Phi}$) and its fluctuation (Φ') as indicated by the following equations [44]:

$$\Phi = \bar{\Phi} + \Phi' \tag{2}$$

$$\bar{\Phi} = \lim_{T \to \infty} \frac{1}{T} \int_{t_0}^{t_0+T} \phi dt \tag{3}$$

For turbulent flow, the averaged part of the concentration can be modeled as [45]:

$$\bar{u}_j \frac{\partial \bar{C}_h}{\partial x_j} = \frac{\partial}{\partial x_k}\left(\left(D_h + D_{h,t}\right) \frac{\partial \bar{C}_h}{\partial x_k}\right) \tag{4}$$

$\bar{C}_h$, $\bar{u}_j$ and $D_{h,t}$ are the averaged concentration, averaged velocity of the j^{th} component, and turbulent diffusion coefficient of saline water, respectively.

The diffusion coefficient of water in saline water, $D_{w,s}(m/s^2)$, can be evaluated using equation (5) [46]:

$$D_h = \frac{(z_+ + |z_-|) D^{Na+} D^{Cl-}}{z_+ D^{Na+} + |z_-| D^{Cl-}} \tag{5}$$

where z_+ and z_- represent the charge of Na^+ and Cl^- ions, respectively (i.e. +1 for Na^+ and -1 for Cl^{-1}) and the *D* values were 1.334×10^{-9} m^2/s for Na^+ and 2.032×10^{-9} m^2/s for Cl^-.

Steady state Reynolds averaged Navier-Stokes (steady state RANS equations) and continuity equations were used to calculate the velocity filed in the concentrated domain [47]:

$$\bar{u}_j \frac{\partial \bar{u}_i}{\partial x_j} = -\frac{1}{\rho}\frac{\partial \bar{P}}{\partial x_i} + \frac{1}{\rho}\frac{\partial}{\partial x_k}\left(\left(\mu_h + \mu_{h,t}\right)\frac{\partial \bar{u}_i}{\partial x_k}\right) + g_i \tag{6}$$

$$\frac{\partial \bar{u}_j}{\partial x_j} = 0 \tag{7}$$

where $\bar{u}_i$, μ_h , $\mu_{h,t}$, $\bar{P}$, and ρ refer to the i^{th} component averaged velocity, fluid dynamic viscosity, turbulent viscosity, average pressure, and density of saline water, respectively. The term g_i is the i^{th} component of gravitational acceleration vector. In this study, the variation of the dynamic viscosity and density due salt concentration and temperature was ignored.

The turbulent steady state energy transport equation used for the concentrated water in the feed side was as follows [47]:

$$\rho C_{ph}\bar{u}_j \frac{\partial \bar{T}_h}{\partial x_j} = \frac{\partial}{\partial x_k}\left(\left(k_h + k_{h,t}\right)\frac{\partial \bar{T}_h}{\partial x_k}\right) \tag{8}$$

where C_{ph} , T_h, k_h, and $k_{h,t}$ are the specific heat capacity of saline water, feed temperature, thermal conductivity and turbulent thermal conductivity, respectively. The total heat flux that saline water received $(q"_{\,Source,h})$ can be calculated using the following Equation (9). It should be noted that this value is the sum of two terms including heat absorption from solar radiation and heat emitted from the membrane surface by radiative heat transfer. Thin acrylic glass is placed at the upper surface of the feed channel to absorb solar radiation. Thus, the temperature distribution through the y-direction of the glass is neglected due to its low thickness.

$$q"_{\,Source,h} = q_{sun}\alpha_g + \varepsilon_m \sigma(\bar{T}_m^4 - \bar{T}_h^4) \tag{9}$$

where T_m , T_h , q_{sun} , α_g , ε_m , and σ are the membrane surface temperature, feed channel temperature, sun flux, absorption coefficient of the used glass, emissivity coefficient of the used membrane, and Boltzmann constant, respectively.

The boundary conditions applied for the mass, momentum, and energy transport equations in the feed side of the membrane are summarized in Table 1.

Table 1. Boundary conditions considered for the numerical simulation of the feed channel.

Position	Mass transfer	Momentum transfer	Heat transfer
$x = 0$	$\bar{C}_h = C_0$	$u = u_0, v = w = 0,$ $P = P_{atm}$	$T_h = T_0$
$x = L$	$(D_h + D_{h,t})\frac{\partial \bar{C}_h}{\partial x} = 0$	$P = P_{atm}$	$(k_h + k_{h,t})\frac{\partial \bar{T}_h}{\partial x} = 0$
$y = y_2$	Mass flux discontinuity	$u = v = w = 0$	Heat flux discontinuity
$y = y_3$	$\frac{\partial \bar{C}_h}{\partial y} = 0$	$u = v = w = 0$	$q''_{Source,h} = q_{sun}\alpha_g + \varepsilon_m \sigma(\bar{T}_m^4 - \bar{T}_h^4)$
$z = 0$	$\frac{\partial \bar{C}_h}{\partial z} = 0$	$u = v = w = 0$	$\frac{\partial \bar{T}_h}{\partial z} = 0$
$z = z_1$	$\frac{\partial \bar{C}_h}{\partial z} = 0$	$u = v = w = 0$	$\frac{\partial \bar{T}_h}{\partial z} = 0$

2.1.2. Membrane

For mass transfer of water vapor through the membrane, the following equation was used [48]:

$$\frac{\partial}{\partial x_k}\left((D_m + D_{m,t})\frac{\partial \bar{C}_m}{\partial x_k}\right) = 0 \quad (10)$$

where the turbulent diffusion coefficient, $D_{m,t}$, was neglected and water vapor diffusion through the membrane pores, D_m, was calculated using the following equations [49]:

$$\frac{1}{D_m} = \frac{\varepsilon}{\zeta}\left(\frac{1}{D_{m,K}} + \frac{1}{D_{m,P}}\right) \quad (11)$$

where ε is the membrane porosity, ζ is the pore tortuosity and the coefficients $D_{m,K}$ and $D_{m,P}$ refer to Knudsen diffusion and Poiseuille type of transport, respectively defined as [50]:

$$D_{m,K} = \frac{2}{3}\, r_p \sqrt{\frac{8RT}{\pi M_w}} \quad (12)$$

$$D_{m,P} = \frac{P\, r_p^2}{8\,\mu} \quad (13)$$

where r_p (m) is pore radius, T (K) is the absolute temperature in the membrane pore, M (kg/mol) is the molecular weight of water vapor, μ is its dynamic viscosity, P is the hydrostatic pressure in the membrane pore and r_p is the membrane pore radius.

Heat transfer through the membrane can be written as:

$$\frac{\partial}{\partial x_k}\left(k_m \frac{\partial \bar{T}_m}{\partial x_k}\right) + q"_{\ Source,m} = 0 \tag{14}$$

where k_m is the thermal conductivity of the membrane matrix, $\bar{T}_m$ is the membrane temperature and $q"_{\ Source,m}$ is the net heat flux received by the membrane.

The thermal conductivity of the membrane (k_m) was calculated by the Maxwell-Eucken considering the thermal conductivity of the thick hydrophobic PVDF layer as reported elsewhere [29]. The Maxwell-Eucken equation was written as [51]:

$$k_m = k_{PVDF} \frac{k_{air} + 2k_{PVDF} - 2\varepsilon(2k_{PVDF} - k_{air})}{k_{air} + 2k_{PVDF} - \varepsilon(2k_{PVDF} - k_{air})} \tag{15}$$

where k_{air} is the thermal conductivity of air and k_{PVDF} is the thermal conductivity of PVDF matrix. In addition, the specific heat at a constant pressure, C_m, and density of the membrane (ρ_m) were estimated using the effective medium theory [52]:

$$C_m = (1 - \varepsilon)C_{PVDF} + \varepsilon C_{air} \tag{16}$$

$$\rho_m = (1 - \varepsilon)\rho_{PVDF} + \varepsilon \rho_{air} \tag{17}$$

The followed boundary conditions for the membrane domain are summarized in the following Table.

Table 2. Boundary conditions used for the numerical simulation of membrane domain.

Position	Mass transfer	Heat transfer
$x = 0$	$\frac{\partial \bar{C}_{wm}}{\partial x} = 0$	$\frac{\partial \bar{T}_m}{\partial x} = 0$
$x = L$	$\frac{\partial \bar{C}_{wm}}{\partial x} = 0$	$\frac{\partial \bar{T}_m}{\partial x} = 0$
$y = y_1$	Flux discontinuity	Flux discontinuity
$y = y_2$	Flux discontinuity	$q"_{\ Source,m} = q_{sun}\alpha_m - \varepsilon_m \sigma(\bar{T}_m^4 - \bar{T}_h^4)$
$z = 0$	$\frac{\partial \bar{C}_{wm}}{\partial z} = 0$	$\frac{\partial \bar{T}_m}{\partial z} = 0$
$z = z_1$	$\frac{\partial \bar{C}_{wm}}{\partial z} = 0$	$\frac{\partial \bar{T}_m}{\partial z} = 0$

2.1.3. Permeate channel

The steady state mass transfer transport equation in turbulent regime was used for modeling the permeate channel domain as follows:

$$\bar{u}_j \frac{\partial \bar{C}_c}{\partial x_j} = \frac{\partial}{\partial x_k}\left(\left(D_c + D_{c,t}\right)\frac{\partial \bar{C}_{wd}}{\partial x_k}\right) \tag{18}$$

where $\bar{u}_j$, $\bar{C}_c$, D_c and $D_{c,t}$ are the *j^th^* component of the averaged velocity, averaged concentration, diffusion coefficient and turbulent diffusion coefficient of distilled water, respectively. The continuity equation and steady state RANS equation in the permeate channel was written as:

$$\bar{u}_j \frac{\partial \bar{u}_i}{\partial x_j} = -\frac{1}{\rho}\frac{\partial \bar{P}}{\partial x_i} + \frac{1}{\rho}\frac{\partial}{\partial x_k}\left(\left(\mu_c + \mu_{c,t}\right)\frac{\partial \bar{u}_i}{\partial x_k}\right) + g_i \tag{19}$$

$$\frac{\partial \bar{u}_j}{\partial x_j} = 0 \tag{20}$$

where $\bar{u}_i$, μ_c , $\mu_{c,t}$, $\bar{P}$, and ρ refer to the i^{th} component of the averaged velocity, fluid dynamic viscosity, turbulent viscosity, average pressure, and density of distilled water, respectively. g_i is the i^{th} component of gravitational acceleration vector. The turbulent steady state energy transport equation used for the permeate is:

$$\rho_c C_{pc} \bar{u}_j \frac{\partial \bar{T}_c}{\partial x_j} = \frac{\partial}{\partial x_k}\left(\left(k_c + k_{c,t}\right)\frac{\partial \bar{T}_c}{\partial x_k}\right) \tag{21}$$

where ρ_c , C_{pc} , T_c, k_c and $k_{c,t}$ are the density, specific heat capacity, temperature, thermal conductivity, and turbulent thermal conductivity of distilled water, respectively.

The following boundary conditions summarized in Table 3 were used to solve the transport equations in the permeate channel.

Table 3. Boundary conditions used for numerical simulation of permeate channel.

Position	Mass transfer	Momentum transfer	Heat transfer
$x = 0$	$(D_c + D_{c,t})\frac{\partial \bar{C}_c}{\partial x} = 0$	$P = P_{atm}$	$(k_c + k_{c,t})\frac{\partial \bar{T}_c}{\partial x} = 0$
$x = L$	$\bar{C}_c = 0$	$u = u_0, v = w = 0$,	$\bar{T}_c = T_{c0}$
$y = 0$	$\frac{\partial \bar{C}_c}{\partial y} = 0$	$u = v = w = 0$	$\frac{\partial \bar{T}_c}{\partial y} = 0$
$y = y_1$	Flux discontinuity	$u = v = w = 0$	Flux discontinuity
$z = 0$	$\frac{\partial \bar{C}_c}{\partial z} = 0$	$u = v = w = 0$	$\frac{\partial \bar{T}_c}{\partial z} = 0$
$z = z_1$	$\frac{\partial \bar{C}_c}{\partial z} = 0$	$u = v = w = 0$	$\frac{\partial \bar{T}_c}{\partial z} = 0$

2.2. Numerical solution and mesh generation

The above mentioned governing equations associated to the feed and permeate channels and membrane domain together with the summarized boundary conditions were solved by COMSOL Multiphysics 5.4. The numerical solver of UMFPACK as a direct solver was applied. For modeling of the turbulence effect, k-ω shear stress transport (SST) model was employed. This model is a two-equations eddy-viscosity which is so practical. The SST is a hybrid model that uses k-ω and k-ε models. The k-ω SST model switches to a k-ε formulation in free-stream to avoid the k-w problem of being sensitive to the inlet free-stream turbulent properties [53].

The software discretized the governing equations by FEM technique on the whole mesh. In fact, with mapping feature, the software can extend the mesh throughout the domains. A mesh of points for each domain has to be specified to have a certain connection between the grids after determining the geometry of the model. Free tetrahedral meshing function generated 2,966,004 elements as shown in Fig. 3. Three meshes were selected to create 1,483,002, 2,966,004 and 5,932,008 elements. The variations between first and second mesh were noticeable, but the change in results between second and third mesh were negligible. Therefore, the second one was used to reduce the computational cost.

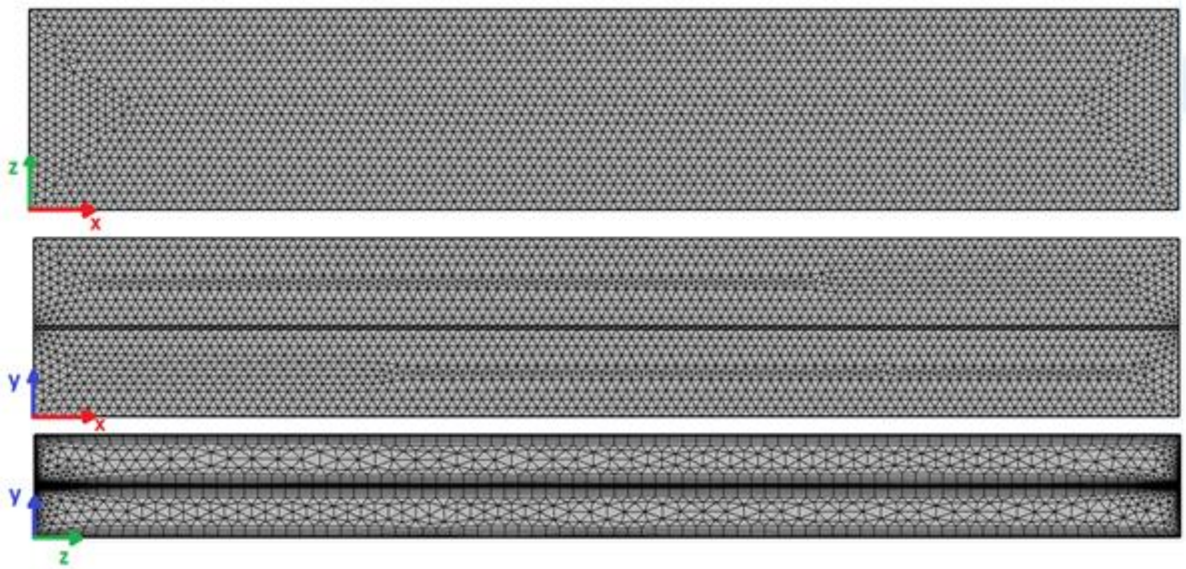

Fig 3. Mesh generation in the feed channel, membrane, and permeate channel domains for numerical simulation.

3. Experimental

3.1. Materials

The materials used for the preparation of the membrane are the hydrophobic polymer PVDF (Zhuzhou Hongda Polymer Materials Co., Ltd.) for the formation of the porous matrix layer, the additive poly(vinyl pyrrolidone) (PVP) for pore formation, the solvent dimethyl formamide (DMF) for polymer solution preparation, the nonwoven polyester (TJ Evrich International Corporation) as a backing material of the membrane, the hydrophilic polymer PAN (Haihang Industry Co., Ltd.) and CB NPs (Shanxi Huachang Chemical Co., Ltd.) with size of 50 nm for the preparation of the photothermal membrane top layer. The PP mesh with an open structure size of 0.011×0.011 inch (Boegger Company) was used to hold the membrane between the feed and permeate channels and to induce turbulent flow condition.

3.2. Membrane preparation

The flat sheet membrane prepared in this study consists of three layers, the nonwoven polyester support to provide the mechanical strength, the porous hydrophobic PVDF layer for water vapor transport, and the top selective PAN layer with dispersed CB NPs, for the absorption of sunlight, coated on the surface of PVDF layer.

The PVDF membrane was prepared by NIPS method. First the PVDF and PVP were dried in oven at 100 ºC. Then, the polymer solution was prepared by mixing the PVDF and PVP in the solvent DMF being the PVDF and PVP concentrations 15 wt.% and 0.5 wt.%, respectively. The mixture was stirred with a magnetic stirrer for 24 h to make sure that a homogeneous solution was formed and subsequently left still for degassing at room temperature for 12 h. Finally, the polymer solution was cast uniformly over the nonwoven polyester by means of a casting knife and the cast film was directly immersed in a distilled water bath for coagulation. The formed membrane was left in distilled water 24 h while water was replaced every 2 h. The obtained PVDF membrane was dried in oven at 40 ºC for 12 h.

The photothermal nanofibrous layer was prepared by electrospinning PAN/CB NPs dispersion over the PVDF supported membrane. PAN is a hydrophilic polymer insoluble in water and therefore suitable for this application.

Electrospinning was performed using the system Fanavaran Nano-Meghyas HV35 0V. To prepare the electrospinning solution, CB NPs were first dispersed in the DMF solvent and the mixture was sonicated for 1 h in an ultrasonic bath (universal DSA 100-SK$_2$-4.0L) to avoid any CB NPs agglomeration. Then PAN was added slowly to the suspension until a final PAN concentration of 15 wt.% was reached. This polymer solution was finally subjected to sonication for 1 h in order to achieve a homogeneous mixture of PAN and CB NPs. Electrospinning, the solution flow rate was 0.5 mL/h, the distance from the syringe tip and the aluminum collector drum was 7 cm, the speed of the collector was 700 rpm, and the electrical voltage was 18 kV. To determine the appropriate concentration of CB NPs in PAN, optical properties of membrane samples prepared with different CB NPs concentrations 1, 3.3 and 5 wt.% were investigated as explained later on. Based on the obtained optical results, the concentration of 3.3 wt.% of CB NPs in PAN was selected as explained later on.

3.3. Membrane Characterization

The surface and cross-section morphology of the prepared membrane samples were studied by scanning electron microscopy (SEM) (Seron Technology, AIS2100, South Korea). In this case, the samples were sputtered with a gold thin layer as reported elsewhere [54]. To prepare the cross-section of the samples, these were fractured in liquid nitrogen.

The optical properties of the membrane samples were studied in terms of their transmittance and reflectance measured by UV-visible diffuse transmittance spectroscopy (DTS) and diffuse reflection spectroscopy (DRS) techniques in the range of 400-900 nm wavelength using the spectrophotometer Avaspec-2048-TEC (Netherlands) [55].

The membrane porosity (ε) was determined by the dry-wet weight method. Samples of 4 cm × 4 cm were first placed in distilled water for 24 h then their surfaces were wiped with a filter paper and weighed with an analytical balance KERN-ALT 310-4. Finally, from the measured dry and wet weights of the samples, the membrane porosity was calculated as follows [56]:

$$\varepsilon = \frac{(m_{wet} - m_{dry})/\rho_{water}}{((m_{wet} - m_{dry})/\rho_{water}) + (m_{dry}/\rho_p)} \tag{22}$$

where m_{dry} and m_{wet} are the dry and wet weights of membrane sample, respectively; ρ_{water} is the water density and ρ_p is the polymer density.

The Guerout-Elford-Ferry equation (Eq. 23) was used to calculate the mean pore radius (r_m) of the membrane samples. In this method, the membrane is subjected to hydraulic pressures and the volume of the permeated distilled water is measured [57].

$$r_m = \sqrt{\frac{(2.9-1.75\varepsilon)8\mu dQ}{\varepsilon * A * \Delta P}} \quad (23)$$

where ε is the membrane porosity, μ is the dynamic viscosity of water (8.9×10^{-4} Pa.s), d is the membrane thickness, Q is the permeate water volume per unit time, A is the effective membrane area, and ΔP is the applied hydrostatic pressure.

The hydrophilic character of the membrane was studied by contact angle measurement (IRASOL CA-500A, Iran). Small droplets of distilled water with volume of 3 µL were deposited on the top membrane surface using a microsyringe and the images were recorded after 30 s. For accuracy, the contact angle was obtained at five different places for a given sample and the average value was calculated.

3.4. PHMD experimental set-up and membrane performance

As mentioned earlier, for this study the PHMD experimental set-up was first designed and the appropriate length of the membrane module was determined by simulation.

The permeate flux (J_p) of the membrane samples in the PHMD system was determined as:

$$J_p = \frac{M}{A \times t} \quad (24)$$

where M is the mass of the collected permeate water, A is the effective membrane area, and t is the operational time.

The electrical conductivity meter SevenMulti (Mettler Toledo, Germany) was used to measure the electrical conductivity of the feed and permeate solutions and the salt rejection was calculated as:

$$R(\%) = \left(1 - \frac{C_c}{C_h}\right) \times 100 \quad (25)$$

where C_c and C_h are the salt concentrations in permeate and feed solutions, respectively.

The thermal efficiency (TE) in the PHMD system was determined as [58]:

$$TE = \frac{j_p\, A\, \Delta H_{v.w}}{A_{active}\, q_{sun}} \quad (26)$$

Where A is the effective area of the membrane, A_{active} is the total area of the membrane that receives sunlight, $\Delta H_{v.w}$ is the water evaporation enthalpy, and q_{sun} is the solar intensity.

The PHMD set-up has two liquid circulating loops, hot feed and cold permeate. The feed side consists of a feed tank with a volume of 10 L, a centrifugal pump (Iwaki MD-20R-NL10), and a pressure gauge (RIGHT PNEUMATICS, RIH) at the inlet of the feed membrane module.

The feed water used in this study was a high NaCl saline aqueous solutions with concentrations range 100 - 190 g/L.

The permeate side consists of a graduated permeate tank of a total volume 1.3 L, a centrifugal pump (HS-100), a heat exchangerto control the temperature . The length, width, and height of both the feed and permeate channels of the membrane module are 66 cm, 15 cm, and 0.35 cm, respectively. The effective area of the membrane in the module is 46 cm × 8 cm. To induce turbulent flows in the feed and permeate channels and hold the membrane due to the long length of the membrane module and low height of channels, the feed and permeate channels were filled with PP mesh grid.

1 mm thick acrylic glass is placed at the upper surface of the feed channel for the direct outdoor sunlight absorption. The pyranometer (Apogee Pyranometer SP-110) was used to measure the solar intensity. The temperatures at the inlets and outlets of the membrane module was measured with thermal probes (PT100) and monitored by a thermocouple data logger. Thermographic images and temperature profiles of the membrane module were obtained using a thermal imaging camera (Testo 881).

Uniform flow distribution in the both the feed and permeate channels took place after 10 min of operation. The duration of each test of saline solution was about 1 h and all tests were repeated three times. The mass of the collected permeate water was determined from the registered volume variation with time in the permeate tank.

The PHMD system in direct contact configuration designed by mechanical desktop software is presented in Fig. 4.

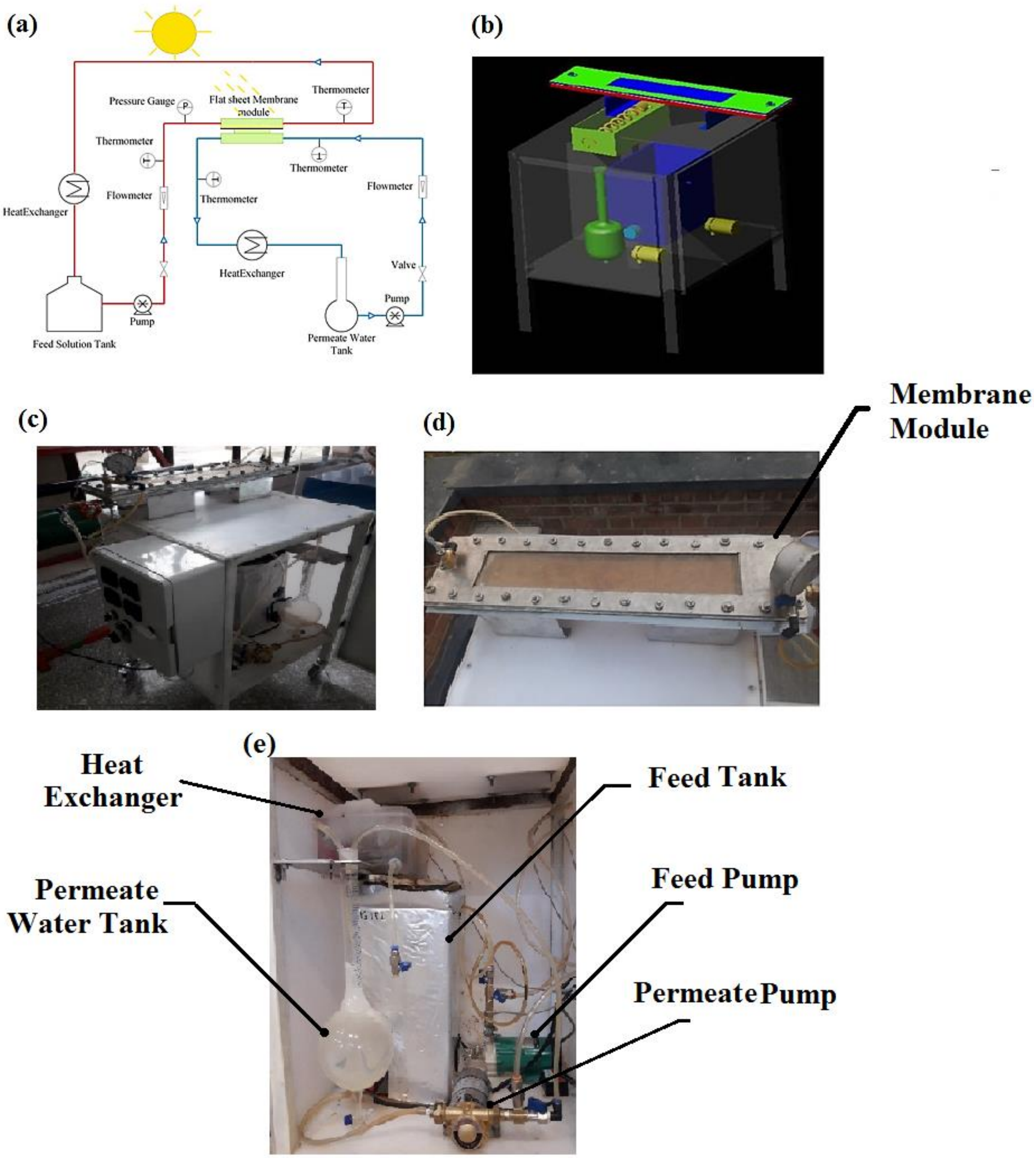

Fig. 4. PHMD experimental set-up: (a) schematic diagram, (b) 3D design by mechanical desktop software, (c) real set-up, and (d) membrane module.

4. Results and discussions

4.1. Appropriate module length

To obtain the appropriate membrane module length, the variation of J_p and *TE* with the module length was simulated for different module lengths and a counter current arrangement of the feed and permeate flows. The results were plotted in Fig. 5. Both J_p and *TE* increased significantly for smaller module lengths than 0.46 m and then tended to asymptotic values showing slight enhancements for larger module lengths. By increasing the module length, the contact time of the feed solution with the membrane and exposure to sunlight became longer resulting in a higher feed temperature as shown in Fig. 5(b) for module lengths below 0.46 m. However, for larger module lengths than 0.46 m, a slight reduction of the feed temperature was observed because of the effect of the permeate that was circulated following a counter current configuration. As it was expected, the permeate temperature was also increased along the membrane module from 0.6 m to 0.28 m approaching finally a steady state value for smaller module lengths. This is due to both the heat transferred by conduction through the membrane and to the heat associated to the generated mass transfer. Therefore, there was no temperature gradient (i.e. difference between feed and permeate temperature) for small module lengths below 0.13 m. Since both the feed and permeate liquids were circulated in a counter current configuration through the membrane module and their temperatures at the inlets of the module were the ambient temperature, the permeate temperature increased along the membrane module reaching a higher value than that of the feed temperature for module lengths below 0.13 m and at the feed module outlet. However, for longer module lengths the temperature gradient started to increase reaching an asymptotic value for module lengths greater than 0.46 m. As consequence, both J_p and *TE* tended to asymptotic values for higher module lengths than 0.46 m (Fig. 5(a)).

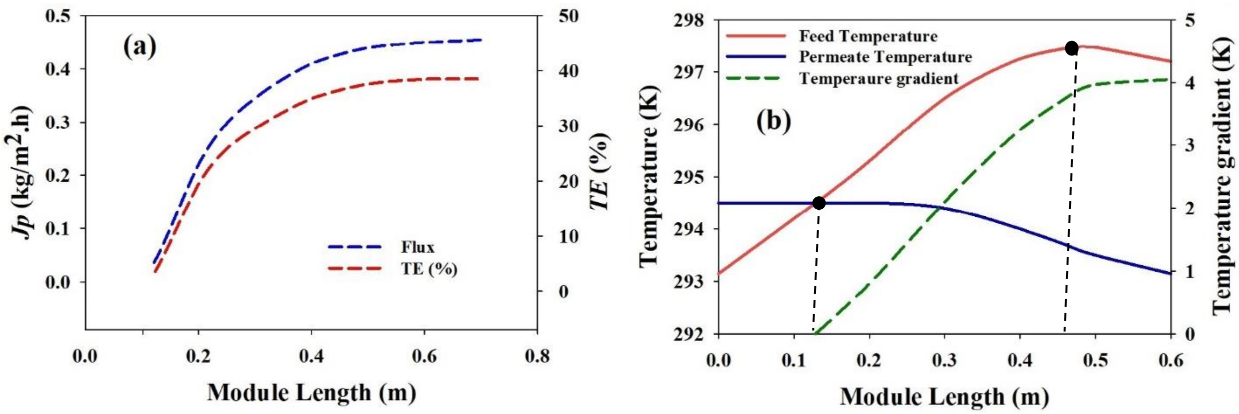

Fig. 5. Effect of the membrane module length on (a) the permeate flux (J_p) and thermal efficiency (*TE*) and (b) temperature gradient in PHMD system ($T_{h,in}$=293.15 K, $T_{c,in}$=293.15 K, T_{amb}=298.15 K, $Q_{h,in}$=0.1 L/min, $Q_{c,in}$=0.6 L/min, q_{sun}=800W/m^2).

Fig. 6 shows the effect of the membrane length on the *Jp* and *TE* of the conventional MD system. To compare the performance of the conventional MD and PHMD systems, both should be operated under the same conditions [29]. According to Fig. 5(b), the feed solution temperature at the inlet of the PHMD system was 293.15 K and reached 297.35 K at the module length of 0.46 m. Therefore, the feed solution temperature at the entrance of the conventional MD system was set to be 297.35 K corresponding to the same input energy in the PHMD system, while the permeate temperature at the inlet of both systems was 293.15 K.

By increasing the module length of the conventional MD system in Fig. 6(a), both *Jp* and *TE* were decreased. However, in the PHMD system, both were increased (Fig. 5(a)). These observed results are due to the significant decline of the feed temperature with the increase of the module length as can be seen in Fig. 6(b) reaching the permeate temperature for a module length of 0.28 m (i.e. no driving force for module lengths greater than this value). As a result, both *Jp* and *TE* were reduced considerably for module lengths below 0.28 m.

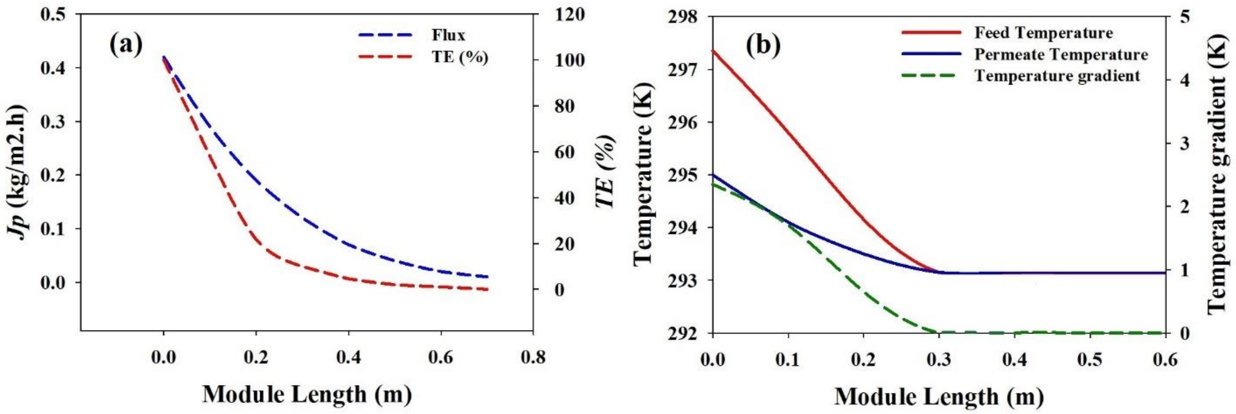

Fig. 6. Effect of the membrane module length on (a) the permeate flux (*J_p*) and thermal efficiency (*TE*) and (b) temperature gradient in conventional MD system ($T_{h,in}$=297.35 K, $T_{c,in}$=293.15 K, T_{amb}=298.15 K, $Q_{h,in}$=0.1 L/min, $Q_{c,in}$=0.6 L/min, q_{sun}=800W/m^2).

4.2. Membrane characterization

Fig. 7 shows the obtained surface and cross-sectional SEM images of the prepared membrane for the PHMD system. As can be seen in Fig. 7(a), the PVDF membrane top surface has a homogenous and porous structure with pore sizes in the range 30 - 40 nm. Its cross-section exhibits a typical asymmetric structure with a thick bottom sponge-like structure, an intermediate thinner macro-void layer and thin denser top layer. Fig. 7(c) shows the nanofibrous network of the PAN/CB NPs top layer prepared by electrospinning. The determined nanofiber diameter was 180 nm. From the cross-section of the prepared membrane, Fig. 7(d), the thickness of the top photothermal layer and the PVDF layer are about 13.5 and 24 µm, respectively.

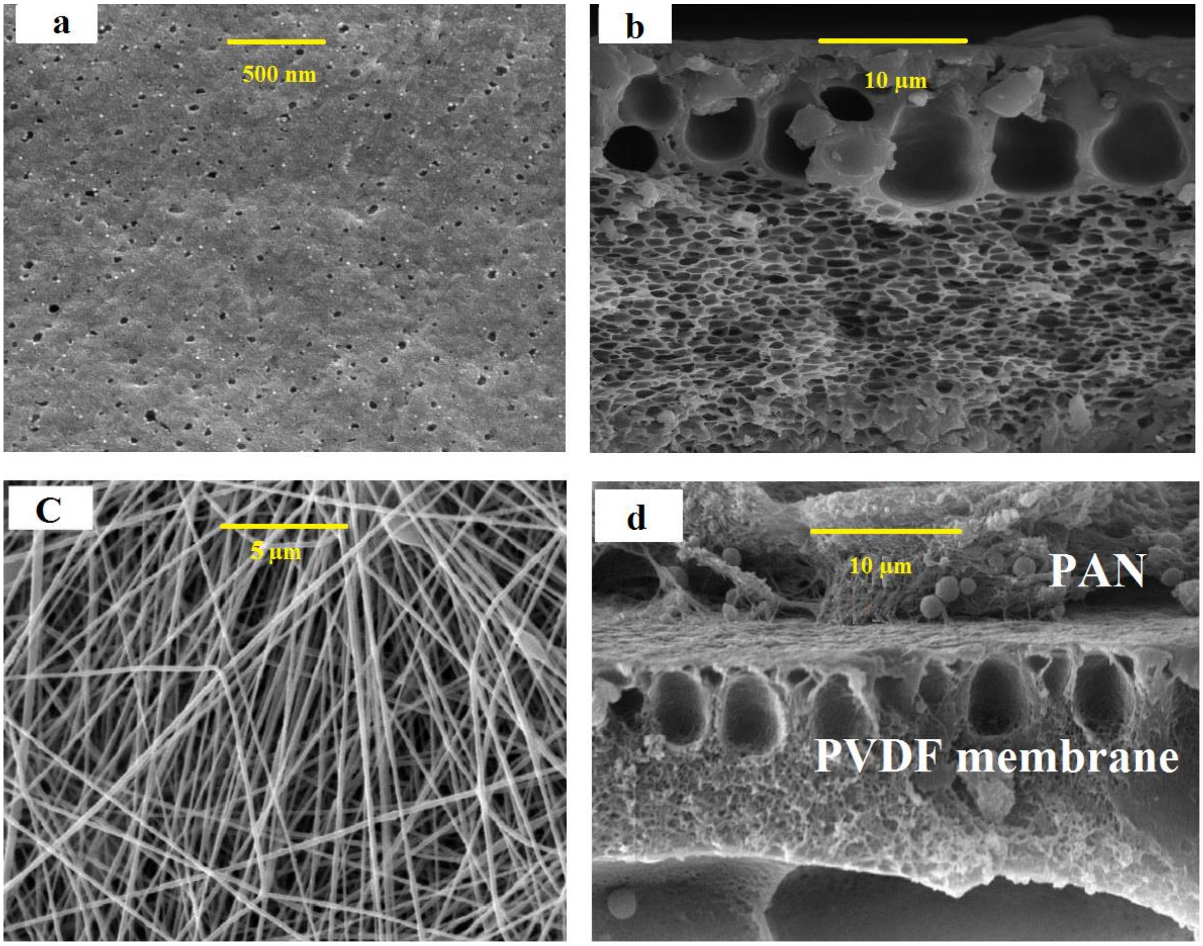

Fig. 7. SEM images of the prepared membrane: (a) top surface of the PVDF membrane, (b) cross-section of the PVDF membrane, (c) electrospun PAN/CB NPs layer (d) cross-section image of the PHMD membrane.

As stated previously, the pore size of the membrane was determined using Eq. (23). The obtained pore size was 25 nm, which is slightly smaller than that determined from the SEM image (Fig. 7(a)) taking into account that the inter-fiber space between nanofibers is greater than that of the PVDF phase inversion membrane [59,60]. In addition, the membrane porosity determined by Eq. (22) was 60%. The measured contact angle of distilled water and 160 g/L NaCl aqueous solution of the PVDF layer was found to be 74º and 81º, respectively (Fig. 8(a) and (b)), while the water contact angle of distilled water and 160 g/L NaCl aqueous solution for the PAN/CB NPs top layer was found to be 49º and 55º, respectively (Fig. 8(c) and (d)).

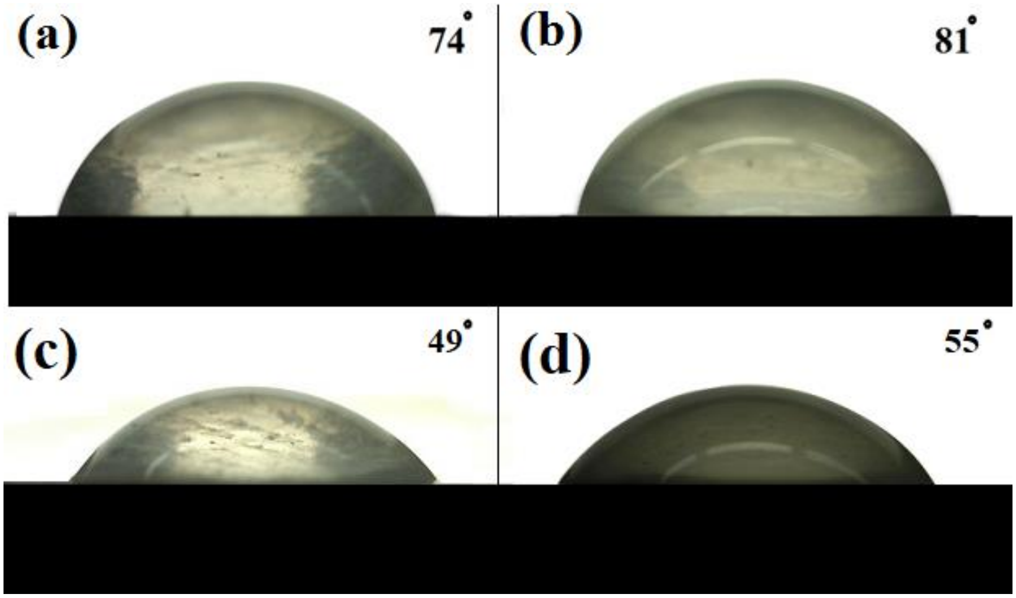

Fig. 8. Contact angle of the membrane, PVDF: (a) deionized water and (b) 160 g/L NaCl aqueous solution, PAN/CB NPs top layer: (c) deionized water and (d) 160 g/L NaCl aqueous solution.

Since the solar irradiation is absorbed by the photothermal PAN/CB NPs layer in the membrane module, the optical properties of the prepared PHMD membranes with different concentrations of CB NPs in PAN (i.e. 1, 3.3 and 5 wt.%) were studied by DRS and DTS techniques. The obtained reflectance and transmittance spectra are shown in Fig. 9. As can be seen, the mean transmission of irradiation sunlight through all investigated PHMD membranes in the visible spectrum were the same (i.e. about 0.2%), but the reflectance of the membranes was different. By increasing the CB NPs concentration from 1 to 3.3 wt.%, the reflectance was decreased from 30.56% to 21.47% (i.e. about 9.9%), which is favorable for the absorption of sunlight by the photothermal layer, while the increase of the CB NPs concentration from 3.3% to 5 wt.%, the reflectance was maintained almost constant. As a result, the concentration of 3.3% of CB NPs in the PAN was selected and used for the preparation of the photothermal PAN layer. The determined absorption efficiency of the tailored triple layered membrane from the scattering reflectance and transmission efficiencies was 78.53% for the membrane prepared with 3.3 wt.% CB NPs in PAN. Dongare et al. [29] measured the reflection of the CB NPs filled PVA layer deposited onto a commercial PVDF and reported a value of 12% for the weight of 3% CB NPs in PVA.

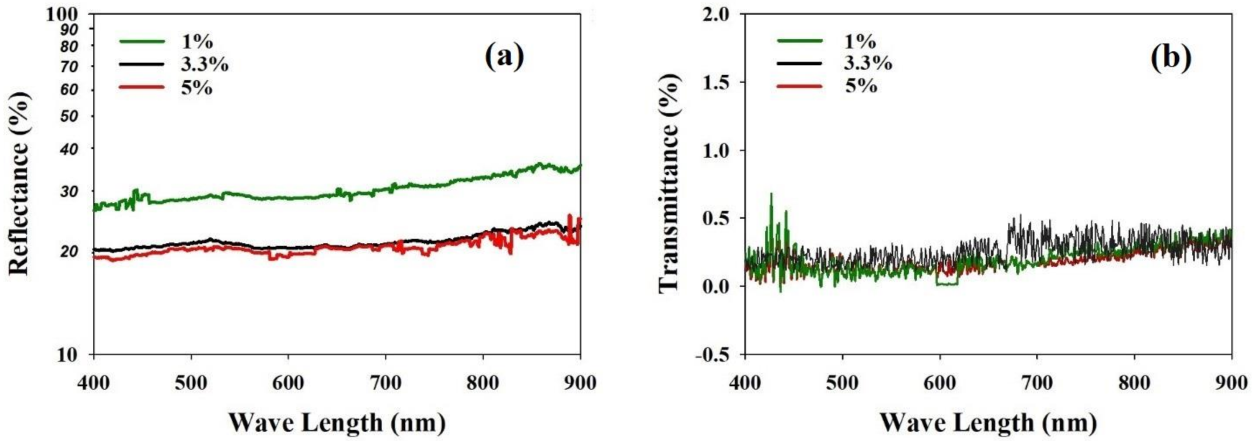

Fig. 9. Optical properties of the PHMD membranes prepared with different concentrations of CB NPs in PAN (a) DRS spectrum and (b) DTS spectrum.

To confirm the photothermal conversion of the proposed PAN/CB NPs top layer of the membrane, thermographic images and temperature profiles were taken at the feed side of the membrane module used in both conventional MD and PHMD systems as shown in Fig. 10 and 11, respectively. In addition, for sake of comparison, thermographic images and temperature profiles of the feed solution circulating through the module without membrane but placed under solar irradiation, and with the PVDF membrane without the photothermal layer as a control membrane, were also presented in Fig. 11.

As it was expected, in Fig. 10 the feed temperature at the exit of the membrane module of the conventional system was lower than that at the inlet because of the heat and mass transfer from the feed to the permeate solution. For instance, in Fig. 10(b) the temperature of the feed solution in the conventional MD system was reduced from 297.35 K to 293.15 K. In this case, the feed temperature at the inlet of the membrane module of the conventional system was set at 297.35 K, which is close that of the feed temperature at the exit of the membrane module of the PHMD system (Fig. 11(b)). However, in Fig. 11, the feed temperature through the membrane module in the PHMD system was increased due to the absorption of solar radiation and the photothermal conversion of the membrane top layer. As can be seen in Fig. 11(b) this feed temperature was increased from 293.15 K to 297.35 K.

The thermographic image and temperature profile of the feed solution under solar irradiation in the module without membrane and circulation of the permeate liquid was also presented in Fig. 11 (case B). In this case, in Fig. 11(b), it can be seen the increase of the feed solution temperature from 293.15 K to 295.25 K due only to solar irradiation. This temperature enhancement was about half that of the feed temperature increment in the PHMD system (case A). Since in the case B the permeate was not circulated through the module, the increase of the feed solution temperature along the module length was not affected by the low temperature of the permeate, the photothermal layer of the membrane or the heat transfer from the feed to the permeate due to the heat transfer by conduction and mass transfer through the membrane that occur in the cases A and C. When using the PVDF membrane without the photothermal layer as a control membrane (case C in Fig. 11), the enhancement of the feed solution temperature was due only to the direct heat of sunlight. In this case the temperature was increased from 293.15 K to 294.35 K, which was about 28% of the temperature increase in the PHMD system (case A). In Fig. 11 (b), for the case C the temperature of the feed solution at the outlet of the module was lower than that in case B. This is mainly due to the effect of the cold permeate temperature. It is therefore worth to say that, other than the effect of the cold permeate temperature and the flow rates of the feed and permeate solutions, the mass transfer through the membrane in the PHMD system is associated not only to the direct sunlight heating of the feed solution but also to the photothermal effect of CB NPs in the PAN layer of the membrane.

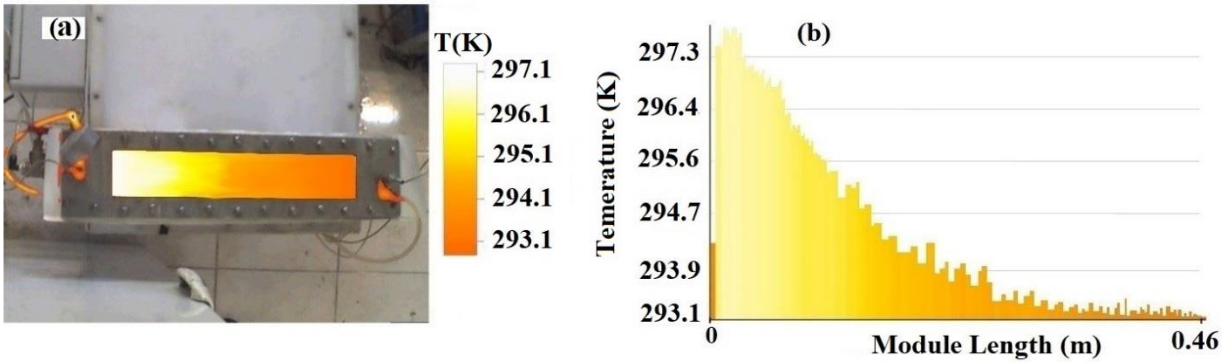

Fig. 10. (a) Thermographic image and (b) temperature profile of the feed channel of the conventional MD system ($T_{h,in}$=297.35 K, $T_{c,in}$=293.15 K, $Q_{h,in}$=0.4 L/min, $Q_{c,in}$=0.4 L/min, NaCl concentration of the feed aqueous solution 160 g/L).

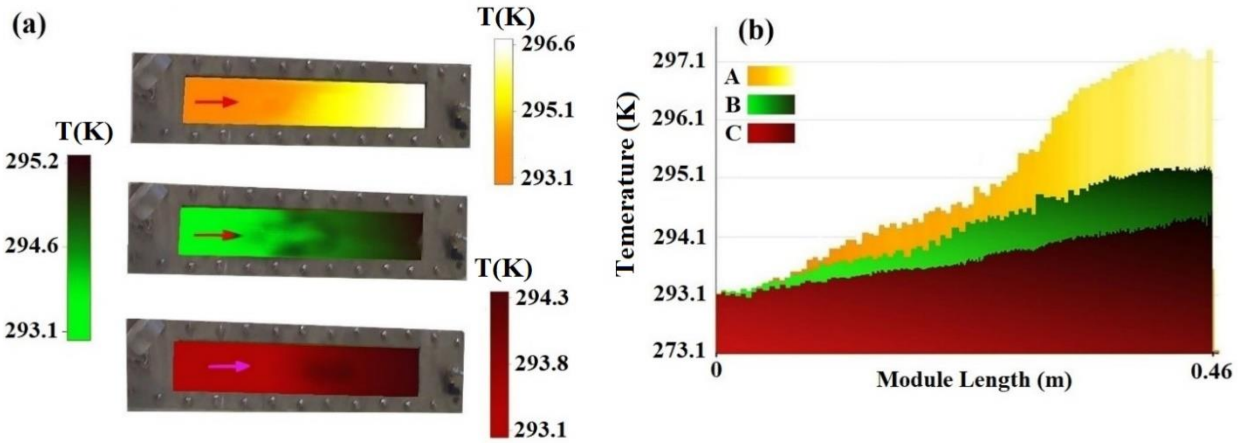

Fig. 11. (a) Thermographic image and (b) temperature profile of A: PHMD system, B: feed solution under solar irradiation in the module without membrane, C: PVDF membrane (as a control membrane) ($T_{h,in}$=293.15 K, $T_{c,in}$=293.15 K, T_{amb}=298.15 K, $Q_{h,in}$ =0.1 L/min, $Q_{c,in}$ =0.6 L/min, q_{sun}=800W/m^2, NaCl concentration of the feed aqueous solution 160 g/L).

4.3. Effect of operating conditions on the membrane performance

4.3.1. Feed water salinity

Fig. 12 shows the effect of the NaCl concentration of the feed aqueous solution on both the permeate flux (J_p) and thermal efficiency (*TE*). With the increase of the salt concentration from 100 to 190 g/L, the permeate flux decreased 33.3%, from 0.51 kg/m^2.h to 0.34 kg/m^2.h while the salt rejection factors were maintained greater than 99.5%. The decrease of the permeate flux is attributed to the reduction of the vapor pressure of water with the increase of NaCl concentration as follows:

$$P_i = P_0\,(1 - x_{NaCl})\,a_w \tag{27}$$

where P_o is the vapor pressure of water, x_{NaCl} is the mole fraction of NaCl in the feed aqueous solution and a_w is water activity that can be determined by the following equation [61]:

$$a_w = 1 - 0.5x_{NaCl} - 10x_{NaCl}^2 \tag{28}$$

The vapor pressure of pure water (P_0) can be estimated by Antoine equation as [62]:

$$P_0 = \exp\left(23.1964 - \frac{3816.44}{T - 46.13}\right) \tag{29}$$

where T is temperature in K and P_0 is in Pa.

In addition, the decrease of the permeate flux is due partly to the increase of the NaCl concentration of the feed solution at the PAN nanofibrous membrane (i.e. external concentration polarization effect) and at the interlayer PAN/PVDF (i.e. internal concentration polarization effect).

The reduction of the permeate flux results in a decrease of the thermal efficiency by 30% when the NaCl concentration was increased from 100 to 190 g/L. This was expected since TE is proportional to the permeate flux as defined in Eq. (26). It is to be noted that the change of the salt concentration in feed aqueous solution, not only affects the vapor pressure but also other thermo-physical properties [63-65]. For instance, the thermal conductivity of the feed solution decreases with the increase of NaCl concentration. However, the applied direct solar heating of the feed solution in the membrane module inhibits the formation of the thermally boundary layer on the feed side of the membrane (Fig. 1) so that the temperature polarization effect is associated only to the thermally boundary layer adjacent to the permeate membrane surface [66]. Therefore, the effect of the reduction of the thermal conductivity of the feed solution due to the increase of the NaCl concentration on the permeate flux and thermal efficiency is not significant compared to the vapor pressure reduction [63-65].

From the developed theoretical model for the PHMD system, both J_p and TE were calculated for the different NaCl concentrations and the results were also plotted in Fig. 12. Good agreement can be seen between the experimental and simulated values being the maximum deviations 4.5% and 1% for J_p and TE, respectively.

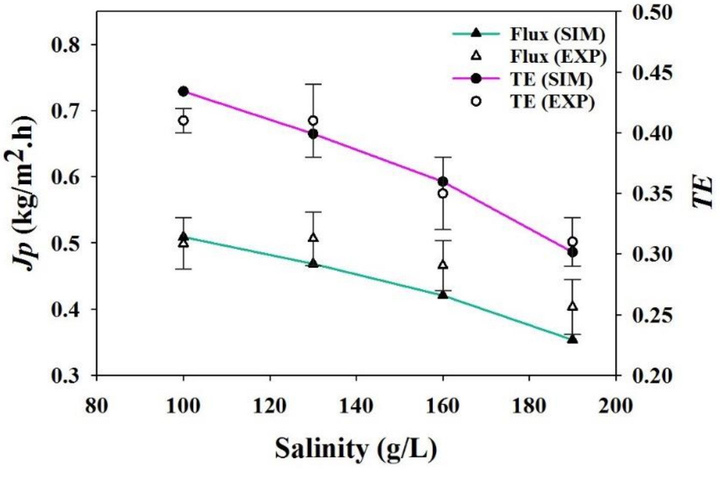

Fig.12. Effect of NaCl concentration y on the experimental and simulated permeate flux (J_p) and thermal efficiency (TE). ($T_{h,in}$=293.15 K, $T_{c,in}$=293.15 K, T_{amb}=298.15 K, $Q_{h,in}$=0.1 L/min, $Q_{c,in}$=0.6 L/min, q_{sun}=800 W/m^2).

4.3.2 Feed and permeate Flow rates

The feed and permeate flow rates are important parameters affecting the performance of MD process [63]. In this study, mesh gridded feed and permeate channels of the membrane module were considered in order to induce turbulent flows at both side of the membrane. The effects of the feed flow rate, ranging from 0.025 L/min to 0.3 L/min, on the permeate flux, thermal efficiency and temperatures at the outlets of the membrane module in the PHMD system are plotted in Fig. 13. As can be seen in Fig. 13(a), both the permeate flux and thermal efficiency decreased significantly for low feed flow rates but leveled off for high feed flow rates and the reduction for permeate flux and thermal efficiency were about 98% and 99%, respectively.

Good agreements were found between the experimental and the simulated values. For sake of comparison, the effect of the feed flow rate on the permeate flux and thermal efficiency of the conventional DCMD process (Fig.1) was also studied under the same operating conditions and the results are presented in Fig. 14. In the conventional DCMD system, where the feed solution is heated outside the membrane module, both the permeate flux and thermal efficiency increased with the increase of the feed flow rate approaching asymptotic values due to the reduction of the temperature and concentration polarization effects. Opposite trends were observed for the PHMD system. In this case, the feed solution with lower flow rates was exposed more time to sunlight in the membrane module and its outlet temperature was higher as indicated in Fig. 13(b). As it is well known, higher feed temperature induces higher vapor pressure resulting in greater driving force for mass transport. With the increase of the feed flow rate, the temperatures of the feed and permeate at the outlets of the membrane module were decreased because the residence time of the feed solution in the membrane module was shorter absorbing less solar radiation (Fig. 13(b)). Compared to the outlet feed temperature, that of the permeate was decreased slightly with the increase of the feed flow rate indicating the predominant effect of the feed temperature and the reduction of the transmembrane vapor pressure together with the permeate flux and the thermal efficiency.

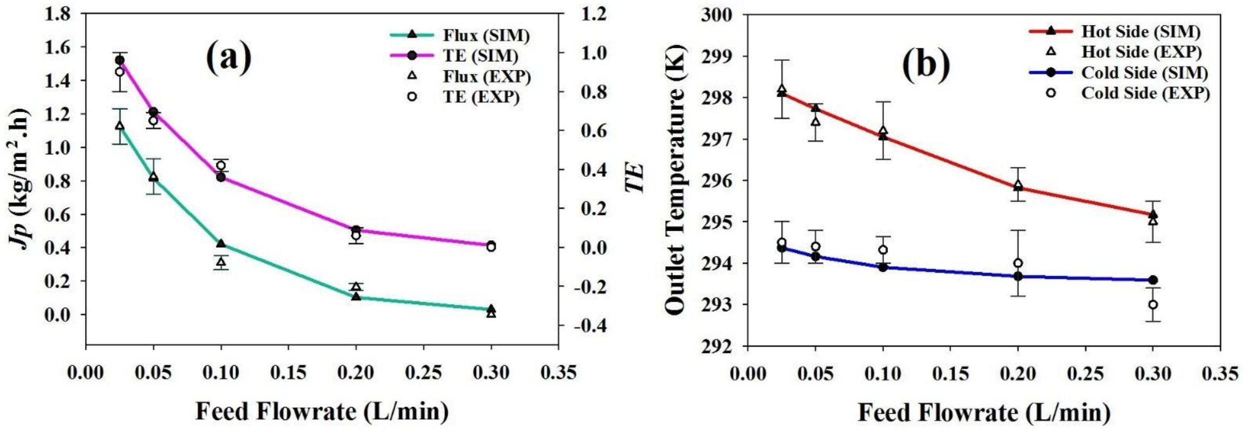

Fig. 13. Effect of the feed flowrate on (a) permeate flux (J_p) and thermal efficiency (*TE*) and (b) temperatures of the feed and permeate at the outlets of the membrane module ($T_{h,in}$=293.15 K, $T_{c,in}$=293.15 K, T_{amb}=298.15 K, $Q_{c,in}$=0.6 L/min, q_{sun}=800 W/m^2, NaCl concentration of the feed aqueous solution 160 g/L).

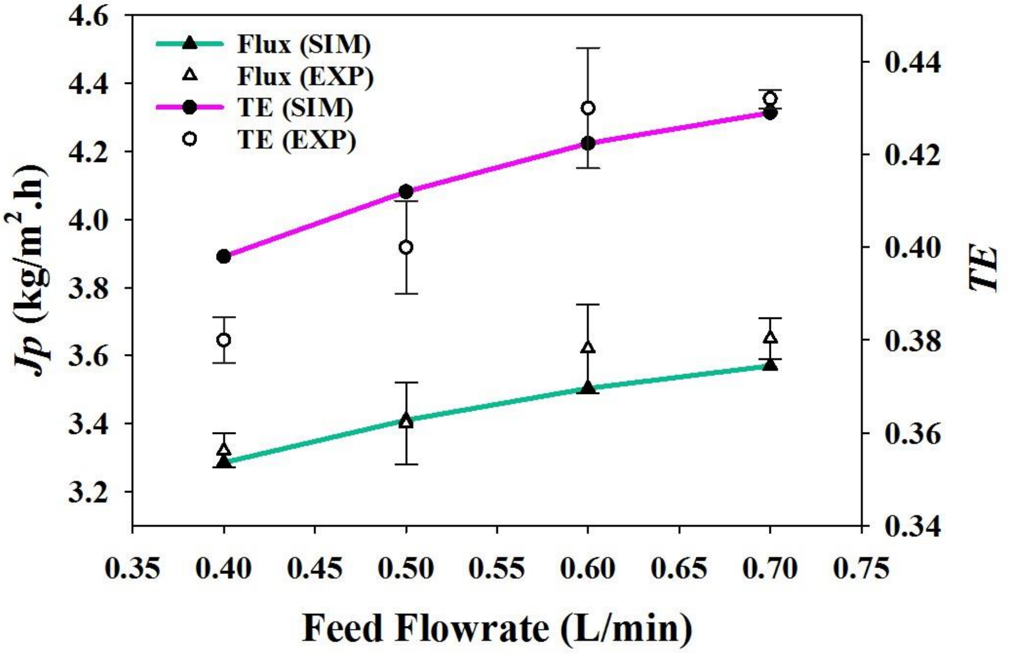

Fig. 14. Effect of the feed flow rate on the permeate flux (J_p) and thermal efficiency (*TE*) in the conventional DCMD process ($T_{h,in}$=323.15 K, $T_{c,in}$=293.15 K, T_{amb}=298.15 K, $Q_{c,in}$=0.4 L/min, NaCl concentration of the feed aqueous solution 160 g/L).

Fig. 15 shows the variation of the permeate flux and thermal efficiency with the permeate flow rate changing from 0.4 L/min to 0.8 L/min. A slight enhancement of the permeate flux, from 0.37 kg/m^2.h to 0.46 kg/m^2.h, was observed with the increase of the permeate flow rate from 0.4 to 0.6 L/min tending to an asymptotic value for higher permeate flow rates up to 0.8 L/min. This improvement of the permeate flux was attributed to the reduction of the temperature polarization effect associated to the reduction of the permeate thermally boundary layer thickness. A similar trend was observed for the thermal efficiency showing an enhancement of 13.8% with the increase of the permeate flux from 0.4 to 0.6 L/min. The maximum error between the experimental and simulated results in Fig. 15 were 3.5% for the permeate flux and 6.4% for the thermal efficiency.

The results of this section elucidated that the feed flow rate had greater effect on the permeate flux and thermal efficiency than the permeate flow rate.

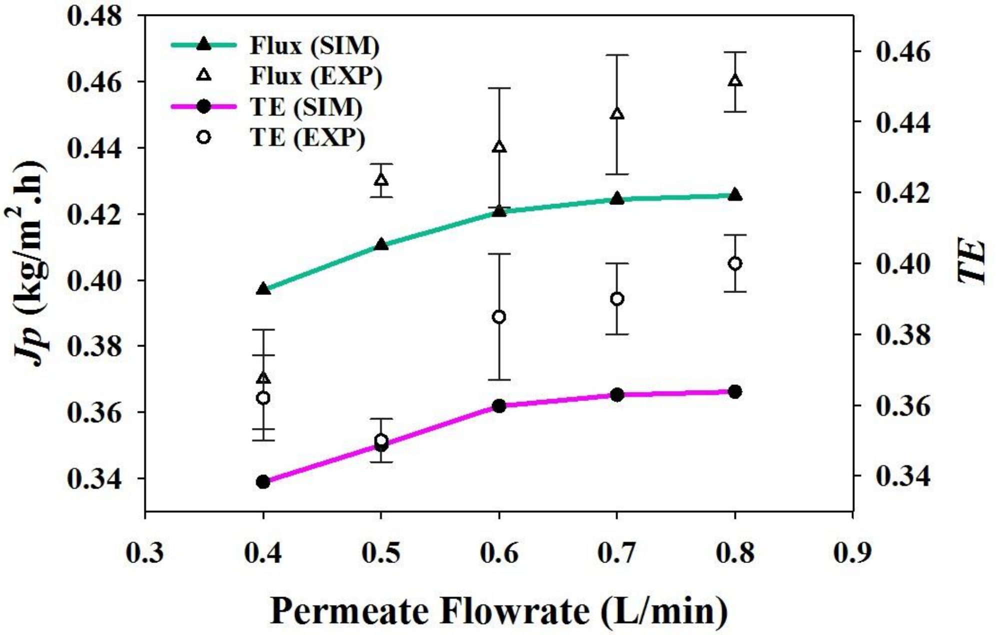

Fig. 15. Effect of the permeate flow rate on the permeate flux (J_p) and thermal efficiency (*TE*). ($T_{h,in}$=293.15 K, $T_{c,in}$=293.15 K, T_{amb}=298.15 K, $Q_{h,in}$=0.1 L/min, q_{sun}=800 W/m^2, NaCl concentration of the feed aqueous solution 160 g/L).

4.3.3 Solar radiation intensity and ambient temperature

The solar radiation intensity is the most important parameter affecting the performance of the developed PHMD system. Fig. 16 shows its effect on the permeate flux, thermal efficiency and the temperatures at the outlet of the membrane module. The increase of solar radiation intensity increased the temperature of the PAN/CB PTs top layer of the membrane inducing a greater driving force for mass transport and consequently higher permeate flux together with an improved thermal efficiency. This is confirmed by the gradual increase of the temperature at the outlet of the membrane module with the increase of solar radiation intensity as can be seen in Fig. 16(b). The increment of the solar radiation intensity from 500 to 1100 W/m^2 resulted in 3.5 times greater permeate flux because of the exponential relationship of the vapor pressure with temperature (Eq. (29)). As stated earlier, a high permeate flux caused a high thermal efficiency because this last term is proportional to the permeate flux. It is also to be noted that the maximum error between the experimental and simulated permeate flux was 1.4% while that of the thermal efficiency was 2%.

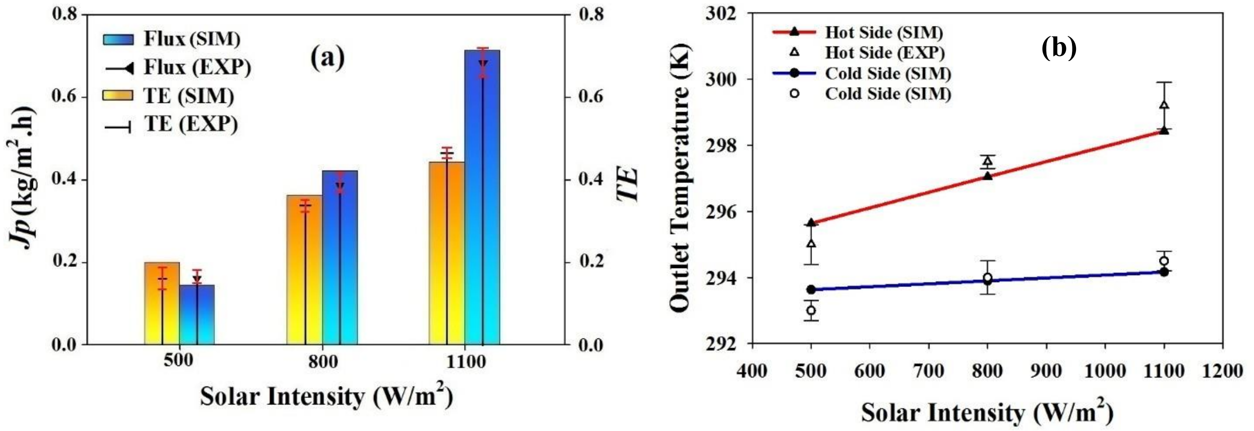

Fig. 16. Effect of the solar radiation intensity on (a) the permeate flux (J_p) and thermal efficiency (TE) and (b) the temperatures of the feed and permeate at the outlets of the membrane module ($T_{h,in}$=293.15 K, $T_{c,in}$=293.15 K, T_{amb}=298.15 K, $Q_{h,in}$=0.1 L/min, $Q_{c,in}$=0.6 L/min, NaCl concentration of the feed aqueous solution 160 g/L).

The effects of the ambient temperature on the permeate flux, thermal efficiency and the temperatures of the feed and permeate at the exits of the membrane module can be seen in Fig. 17. With the increase of the ambient temperature from 293 K to 313 K, both the permeate flux and the thermal efficiency were improved but only slight enhancements were observed, which were 41% and 30 % for the permeate flux and thermal efficiency, respectively. A higher ambient temperature resulted in a greater feed temperature as can be seen in Fig. 17(b) and the subsequent enhancement of the driving force taking into account the slight increase of the permeate temperature due to the heat transfer through the membrane associated to both the heat transfer by conduction through the membrane matrix and the heat associated to mass transfer through the membrane pores. It must be stated that good agreements were obtained between the experimental and simulated values as can be seen in Fig. 17. The registered error between the experimental and simulated results for the permeate flux and thermal efficiency were lower than 3.2% and 0.2%, respectively.

It must be mentioned that the use of PAN layer and the mesh-gridded channels in the PHMD system improved the permeate flux by 68% (i.e. 0.42 kg/m^{2}h) compared to that reported by Dongare et al. [29] for a membrane module with a 46 cm length, CBNPs in PVA as a photothermal layer and laminar flow regime (i.e. a permeate flux of 0.25 kg/m^{2}h).

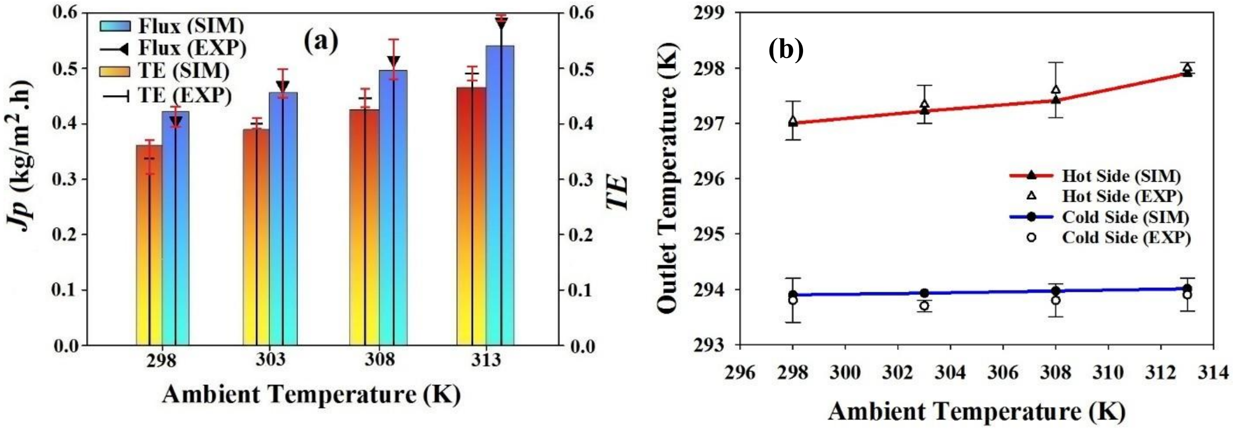

Fig. 17. Effect of the ambient temperature on (a) the permeate flux (J_p) and thermal efficiency (TE) and (b) the temperatures of the feed and permeate at the outlets of the membrane module ($T_{h,in}$=293.15 K, $T_{c,in}$=293.15 K, $Q_{h,in}$ =0.1 L/min, $Q_{c,in}$=0.6 L/min, q_{sun}=800 W/m^2, NaCl concentration of the feed aqueous solution 160 g/L).

5. Conclusions

Since MD technology is an energy-intensive desalination system, the use of renewable energies such as solar energy is essential for its adequate development and implementation. In this study, we designed and fabricated a solar-driven PHMD system for desalination by direct contact membrane distillation (DCMD) of high saline waters. A triple layered membrane consisting of a photothermal top layer composed of PAN with dispersed CB NPs, a phase inversion PVDF porous membrane as an intermediate layer and a polyester support. PP mesh was used to hold the membrane between the feed and permeate channels and to induce turbulent flow conditions. The high saline feed aqueous solution was heated while circulating through the membrane module by means of the photothermal PAN/CB NPs layer of the membrane. The tailored membrane exhibited a mean pore size of 25 nm, a porosity of 60%, a total thickness of 24 µm for PVDF layer and for photothermal top layer (PAN) thickness of 13.5 µm, and good optical properties for photothermal conversion (i.e. 21.53%, 0.2% and 78.53% mean reflection, transmission and absorption efficiency of irradiation sunlight in the visible spectrum). CFD technique was used to model the counter-current PHMD membrane module and membrane length of 46 cm was obtained. Therefore, the PHMD membrane module with a length of 66 cm and an effective membrane length of 46 cm was fabricated.

The effects of the feed water concentration, feed and the permeate flow rates, solar radiation intensity and ambient temperature on the J_p, *TE* and temperatures of the feed and permeate at the outlets of the membrane modules were studied. The following results were observed.

- Rising the feed water salinity from 100 g/L to 190 g/L, resulted in a decline of both J_p and *TE* with 33.3% and 30%, respectively.
- Unlike the conventional MD, in the PHMD system both J_p and *TE* were reduced with the increase of the feed flow rate tending to asymptotic values. This due to the fact that the feed solution with lower flow rates was exposed more time to sunlight in the membrane module resulting in higher temperatures and driving force for mass transport as consequence.
- Increasing the permeate flow rate improved slightly the performance of the PHMD system due to the reduction of the temperature polarization effect in the permeate side.

- The solar radiation intensity exerted significant effects on both J_p and *TE*. By intensifying the solar radiation intensity from 500 W/m^2 to 1100 W/m^2, J_p and *TE* were increased by 257% and 166%, respectively.
- Increasing the ambient temperature from 298 K to 313 K, resulted in 41% and 30% improvement of J_p and *TE*, respectively.
- Very good agreements were observed between the experimental results and the simulation ones (Jp, TE and temperatures of the feed and permeate at the outlets of the membrane module).

Acknowledgements:

M. Khayet gratefully acknowledges the financial support of the FEI Europeos - Unidad de Investigación of the University Complutense of Madrid (UCM) through the project FEI-EU-21-04. All authors would like thank Sharif Membrane Technology Center for providing materials and equipment for this project.

Nomenclature

A: membrane area
a_w: water activity
C_h: feed solution concentration
C_c: permeate solution concentration
$\bar{C}_h$: average part of saline concentration
$\bar{C}_c$: averaged part of diluted concentration
C_h': fluctuated part of saline concentration
C_m: specific heat at constant pressure of membrane
C_{PVDF}: specific heat at constant pressure of PVDF
C_{air}: specific heat at constant pressure of air
C_{pc}: specific heat capacity of permeate solution
C_{ph}: specific heat capacity of feed solution
d: thickness
D_h: diffusion coefficient of saline water
$D_{h,t}$: turbulent diffusion coefficient of saline water
D_c: diffusion coefficient of permeate solution
$D_{c,t}$: turbulent diffusion coefficient of permeate solution
D_m: membrane diffusion coefficient
$D_{m,t}$: membrane turbulent diffusion coefficient
$D_{w,air}$: diffusion of water vapor in air
g_i: gravitational acceleration

$H_{v.w}$: water vapor enthalpy
J_P: permeate flux
k_h: thermal conductivity of saline water
$k_{h,t}$: turbulent thermal conductivity of saline water
k_c: thermal conductivity of permeate of permeate solution
$k_{c,t}$: turbulent thermal conductivity of permeate solution
k_m : thermal conductivity of solid membrane
k_{air}: thermal conductivity of air
k_{PVDF}: thermal conductivity of PVDF
M: mass of collected permeate water
m_{dry}: dry of membrane sample
m_{wet}: wet weight of membrane sample
$\bar{P}$: average part of pressure
P_i: vapor pressure of water
P_0: vapor pressure of pure water
Q: flowrate
$q"_{Source,h}$: total heat flux that saline water receives
$q"_{Source,m}$: net heat flux that membrane receives
q_{sun}: solar intensity
r: pore size
r_m: mean pore radius
t: operational time
T: temperature
TE: thermal efficiency
T_m: membrane temperature
$\bar{T}_m$: average part of membrane temperature
T_g: glass temperature
u_j: velocity of jth component
$\bar{u}_j$: averaged velocity of jth component
u: x-direction velocity
w: z-direction velocity
x_{NaCl}: the mole fraction of NaCl solution
y: y-direction velocity

Subscripts
amb: ambient
b: bulk
c: permeate solution
g: glass
h: feed solution
i: free index
in: inlet
j: dummy index
k: dummy index
m: membrane

p: polymer
$PVDF$: polyvinylidene Fluoride
s: saline water
sun: solar
t: turbulent
v: vapor
w: water

Greek letter

ε_m: emissivity coefficient of membrane
ρ: density
ρ_p: polymer density
α: absorption coefficient
ζ_+: charge of Na+ ion
ζ_-: charge of Cl- ion
ε: porosity
μ: dynamic viscosity
μ_h: fluid dynamic viscosity of feed solution
$\mu_{h,t}$: turbulent viscosity of feed solution
μ_c: fluid dynamic viscosity of permeate solution
$\mu_{c,t}$: turbulent dynamic viscosity of permeate solution

Abbreviations:

DCMD: direct contact membrane distillation
DMF: dimethylformamide
DRS: diffuse reflection spectroscopy
DTS: diffuse transmittance spectroscopy
FEM: finite element method
MD: membrane distillation
PHGMD: photothermally heated and mesh-gridded membrane distillation
PAN: polyacrylonitrile
PVDF: polyvinylidene Fluoride
PVP: poly(vinyl pyrrolidone)
RO: reverse osmosis
SEM: scanning electron microscopy

References

[1] Y. H. Teow, A. W. Mohammad, New generation nanomaterials for water desalination: a review, Desalination 451 (2019) 2-17.

[2] K. Wang, A. A. Abdalla, M. A. Khaleel, N. Hilal, M. K. Khraisheh, Mechanical properties of water desalination and wastewater treatment membranes, Desalination 401 (2017) 190-205.

[3] M. Qasim, M. Badrelzaman, N. N. Darwish, N. A. Darwish, N. Hilal, Reverse osmosis desalination: A state-of-the-art review, Desalination 459 (2019) 59-104.

[4] M. Asadollahi, D. Bastani, S. A. Musavi, Enhancement of surface properties and performance of reverse osmosis membranes after surface modification: a review, Desalination 420 (2017) 330-383.

[5] F. E. Ahmed, B. S. Lalia, R. Hashaikeh, N. Hilal, Alternative heating techniques in membrane distillation: A review, Desalination 496 (2020) 114713.

[6] M. Khayet, T. Matsuura, Introduction to membrane distillation. In: Khayet, M., Matsuura, T. (Eds.), Membrane Distillation, Elsevier, 2011, pp. 1-16.

[7] F. E. Ahmed, R. Hashaikeh, N. Hilal, Hybrid technologies: The future of energy efficient desalination-A review, Desalination 495 (2020) 114659.

[8] K. Sardaria, P. Fyfeb, S. R. Wickramasinghe, Integrated electrocoagulation-Forward osmosis-Membrane distillation for sustainable water recovery from hydraulic fracturing produced water, J. Membr. Sci. 574 (2019) 325-337.

[9] B. B. Ashoor, S. Mansour, A. Giwa, V. Dufour, S. W. Hasan, Principles and applications of direct contact membrane distillation (DCMD): A comprehensive review, Desalination 398 (2016) 222-246.

[10] J. A. Sanmartino, M. Khayet, M. C. García-Payo, Desalination by Membrane Distillation, in: N. P. Hankins, R. Singh, Emerging Membrane Technology for Sustainable Water Treatment, Elsevier, 2016, pp. 77-109.

[11] M. Rezaei, D. M. Warsinger, J. H. Lienhard V, M. C. Duke, T. Matsuura, W. M. Samhaber,Wetting phenomenon in membrane distillation: mechanisms, reversal, and prevention, Water Res. 139 (2018) 329-352.

[12] A. Anvari, A. A. Yancheshme, K. M. Kekre, A. Ronen, State-of-the-art methods for overcoming temperature polarization in membrane distillation process: a review, J. Membr. Sci. 616 (2020) 118413.

[13] Z. Liu, Q. Pan, C. Xiao, Preparation and vacuum membrane distillation performance of a silane coupling agent-modified polypropylene hollow fiber membrane, Desalination 468 (2019) 114060.

[14] Z. Xu, Z. Liu, P. Song, C. Xiao, Fabrication of super-hydrophobic polypropylene hollow fiber membrane and its application in membrane distillation, Desalination 414 (2017) 10-17.

[15] C. Su, Y. Li, H. Cao, C. Lu, Y. Li, J. Chang, F. Duan, Novel PTFE hollow fiber membrane fabricated by emulsion electrospinning and sintering for membrane distillation, J. Membr. Sci. 583 (2019) 200-208.

[16] A. Bottino, A. Comite, C. Costa, M. Pagliero, Novel hydrophobic PVDF membranes prepared by nonsolvent induced phase separation for membrane distillation, J. Membr. Sci. 596 (2020) 117575.

[17] Z. Anari, A. Sengupta, K, Sardari, S. R. Wickramasinghe, Surface modification of PVDF membranes for treating produced waters by direct contact membrane distillation, Sep. Purif. Technol. 224 (2019) 388-396.

[18] S. Munirasu, F. Banat, A. A. Durrani, M. A. Haija, Intrinsically superhydrophobic PVDF membrane by phase inversion for membrane distillation, Desalination 417 (2017) 77-86.

[19] L. Yue, J. Cailan, P. Yuelian, A. Quanfu, C. Zhengping, Z. Jiacheng, G. Lei, W. Shaobin, Fabrication of PVDF hollow fiber membranes via integrated phase separation for membrane distillation, J. Taiwan Inst. Chem. Eng. 95 (2019) 487-494.

[20] K. Zhani, K. Zarzoum, H. B. Bacha, J. Koschikowski, D. Pfeifle, Autonomous solar powered membrane distillation systems: state of the art. Desalin. Water Treat. 57 (2016) 23038-23051.

[21] M. Khayet, Solar desalination by membrane distillation: Dispersion in energy consumption analysis and water production costs (a review), Desalination 308 (2013) 89-101.

[22] N. Palanisami, K. He, I. S. Moon, Utilization of solar energy for direct contact membrane distillation process: an experimental study for desalination of real seawater, Korean J. Chem. Eng. 31 (2014) 155-161.

[23] A. Shafieian, M. Khiadani, A novel solar-driven direct contact membrane-based water desalination system, Energy Convers. Manag. 199 (2019) 112055.

[24] T. C. Chen, C. D. Ho, Immediate assisted solar direct contact membrane distillation in saline water desalination, J. Memb. Sci. 358 (2010) 122-130.

[25] G. Xue, Q. Chen, S. Lin, J. Duan, P. Yang, K. Liu, J. Li, J. Zhou, Highly Efficient Water Harvesting with Optimized Solar Thermal Membrane Distillation Device, Glob. Chall. 2 (2018) 1800001.

[26] A. Bamasag, T. Alqahtani, S. Sinha, N. Ghaffour, P. Phelan, Experimental investigation of a solar-heated direct contact membrane distillation system using evacuated tube collectors, Desalination 487 (2020) 114497.

[27] Y. Zhang, L. Liu, K. Li, D. Hou, J. Wang, Enhancement of energy utilization using nanofluid

in solar powered membrane distillation, Chemosphere 212 (2018) 554-562.

[28] A. Politano, G. Di Profio, E. Fontananova, V. Sanna, A. Cupolillo, E. Curcio, Overcoming temperature polarization in membrane distillation by thermoplasmonic effects activated by Ag nanofillers in polymeric membranes, Desalination 451 (2019) 192-199.

[29] P. D. Dongare, A. Alabastri, S. Pedersen, K. R. Zodrow, N. J. Hogan, O. Neumann, J. Wud, T. Wang, A. Deshmukh, M. Elimelech, Q. Li, P. Nordlander, N. J. Halas, Nanophotonics enabled solar membrane distillation for off-grid water purification, Proc. Natl. Acad. Sci. U. S. A. 114 (2017) 6936-6941.

[30] J. Wu, K. R. Zodrow, P. B. Szemraj, Q. Li, Photothermal nanocomposite membranes for direct solar membrane distillation, J. Mater. Chem. A. 5 (2017) 23712-23719.

[31] X. Wu, Q. Jiang, D. Ghim, S. Singamaneni, Y. S. Jun, Localized heating with a photothermal polydopamine coating facilitates a novel membrane distillation process, J. Mater. Chem. A. 6 (2018) 18799-18807.

[32] K. Charfi, M. Khayet, M.J. Safi, Numerical simulation and experimental studies on heat and mass transfer using sweeping gas membrane distillation, Desalination, 259 (1-3) (2010) 84-96.

[33] M. Khayet, A.O. Imdakm, T. Matsuura, Monte Carlo simulation and experimental heat and mass transfer in direct contact membrane distillation, Int. J. Heat and Mass Transfer, 53 (7-8) (2010) 1249-1259.

[34] M. Essalhi, M. Khayet, Self-sustained webs of polyvinylidene fluoride electrospun nanofibers at different electrospinning times: 2. Theoretical analysis, polarization effects and thermal efficiency, J. Membrane Sci., 433 (2013) 180-191.

[35] J. Lou, J. Vanneste, S. C. DeCaluwe, T. Y. Cath, N. Tilton, Computational fluid dynamics simulations of polarization phenomena in direct contact membrane distillation, J. Membr. Sci. 591 (2019) 117150.

[36] P. Yazgan-Birgi, M. I. H. Ali, H. A. Arafat, Comparative performance assessment of flat sheet and hollow fiber DCMD processes using CFD modeling, Sep. Purif. Technol. 212 (2019) 709-722.

[37] V. Perfilov, A. Ali, V. Fila, A general predictive model for direct contact membrane distillation, Desalination 445 (2018) 181-196.

[38] M. Hasanizadeh, P. Jafari, B. Farshighazani, M.K. Moraveji, CFD simulation of heat and mass transport for water transfer through hydrophilic membrane in direct-contact membrane distillation process, Desalin. Water Treat. 57 (39) (2016) 18109-18119.

[39] M. Khayet, Membranes and theoretical modeling of membrane distillation: A review, Advances in Colloid and Interface Science 164 (2011) 56-88.

[40] I. Janajreh, D. Suwwan, R. Hashaikeh, Assessment of direct contact membrane distillation under different configurations, velocities and membrane properties, Appl. Energy 185 (Part 2) (2017) 2058-2073.

[41] D. J. Park, E. Norouzi, C. Parkb, Experimentally-validated computational simulation of direct contact membrane distillation performance, Int. J. Heat Mass Tran. 129 (2019) 1031-1042.

[42] M. Shokrollahi, M. Rezakazemi, M. Younas, Producing water from saline streams using membrane distillation: Modeling and optimization using CFD and design expert, Int. J. Energy Res. 44 (2020) 8841-8853.

[43] M. Rezakazemi, CFD simulation of seawater purification using direct contact membrane desalination (DCMD) system, Desalination 443 (2018) 323-332.

[44] F. M. White, I. Corfield, Viscous fluid flow. Vol. 3. New York: McGraw-Hill, 2006

[45] S. Soukane, M. W. Naceur, L. Francis, A. Alsaadi, N. Ghaffour, Effect of feed flow pattern on the distribution of permeate fluxes in desalination by direct contact membrane distillation, Desalination 418 (2017) 43-59.

[46] D. R. Lide, CRC handbook of chemistry and physics. Vol. 85. 2004: CRC press.

[47] V. S. Arpaci, P. S. Larsen, Convection heat transfer, Prentice Hall, 1984

[48] M. Ghadiri, S. Fakhri, S. Shirazian, Modeling and CFD simulation of water desalination using nanoporous membrane contactors, Ind. Eng. Chem. Res., 52 (2013) 3490-3498.

[49] B. Tjaden, S. J. Cooper, D. J. L. Brett, D. Kramer, P. R. Shearing, On the origin and application of the Bruggeman correlation for analysing transport phenomena in electrochemical systems, Curr. Opin. Chem. Eng. 12 (2016) 44-51.

[50] V. Karanikola, A. F. Corral, H. Jiang, A. E. Sáez, W. P. Ela, R. G. Arnold, Effects of membrane structure and operational variables on membrane distillation performance, J. Membr. Sci. 524 (2017) 87-96.

[51] M. Wang, N. Pan, Predictions of effective physical properties of complex multiphase materials. Mater. Sci. Eng. R. Rep. 63 (2008) 1-30.

[52] X.–Q. Wang, A. S. Mujumdar, A review on nanofluids-part I: theoretical and numerical investigations, Braz. J. Chem. Eng. 25 (2008) 613-630.

[53] U. F. Alqsair, A. M. Alshwairekh, A.M. Alwatban, A. Oztekin, Computational study of sweeping gas membrane distillation process–Flux performance and polarization characteristics, Desalination 485 (2020) 114444.

[54] M. Ganj, M. Asadollahi, S. A. Mousavi, D. Bastani, F. Aghaeifard, Surface modification of polysulfone ultrafiltration membranes by free radical graft polymerization of acrylic acid using

response surface methodology, J. Polym. Res. 26, 231 (2019) 1-19.

[55] N. J. Hogan, A. S. Urban, C. Ayala-Orozco, A. Pimpinelli, P. Nordlander, N. J. Halas, Nanoparticles heat through light localization, Nano Lett. 14 (2014) 4640–4645.

[56] S. Santoro, I. M. Vidorreta, V. Sebastian, A. Moro, I. M. Coelhoso, C. A. M. Portugal, J. C. Lima, G. Desiderio, G. Lombardo, E. Drioli, R. Mallada, J. G. Crespo, A. Criscuoli, A. Figoli, A non-invasive optical method for mapping temperature polarization in direct contact membrane distillation, J. Membr. Sci. 536 (2017) 156-166.

[57] M. S. Islam, K. Touati, M. S. Rahaman, Feasibility of a hybrid membrane-based process (MF-FO-MD) for fracking wastewater treatment, Sep. Purif. Technol. 229 (2019) 115802.

[58] R. Ullah, M. Khraisheh, R. J. Esteves, J. T. McLeskey Jr, M. AlGhouti, M. Gad-el-Hak, H. V. Tafreshi, Energy efficiency of direct contact membrane distillation, Desalination 433 (2018) 56-67.

[59] M. Khayet, M.C. García-Payo, L. García-Fernández, J. Contreras-Martínez, Dual-layered electrospun nanofibrous membranes for membrane distillation, Desalination, 426 (2018) 174-184.

[60] M. Essalhi, M. Khayet, C. Cojocaru, M.C. García-Payo, P. Arribas, Response surface modeling and optimization of electrospun nanofiber membranes, the Open Nanoscience J., 7 (2013) 8-17.

[61] T.-C. Chen, C.-D. Ho, H.-M. Yeh, Theoretical modeling and experimental analysis of direct contact membrane distillation, J. Membr. Sci. 330 (1) (2009) 279-287.

[62] M. A. E.-R. Abu-Zeid, Y. Zhang, H. Dong, L. Zhang, H.-L. Chen, L. Hou, A comprehensive review of vacuum membrane distillation technique, Desalination 356 (2015) 1-14.

[63] M. Khayet, T. Matsuura, Membrane distillation: Principles and application, Elsevier, 2011.

[64] M.M. Generous, N.A.A. Qasem, B.A. Qureshi, S.M. Zubair, A comprehensive review of saline water correlations and data - Part I: thermophysical properties, Arab. J. Sci, Eng. 45 (2020) 8817-8876.

[65] N.A.A. Qasem, M.M. Generous, B.A. Qureshi, S.M. Zubair, A comprehensive review of saline water correlations and data - Part II: thermophysical properties. Arab. J. Sci, Eng. 46 (2021) 1941-1979.

[66] M. Khayet, M.P. Godino, J.I. Mengual, Study of asymmetric polarization in direct contact membrane distillation, Sep. Sci. Tech. 39 (1) (2005) 125-147.